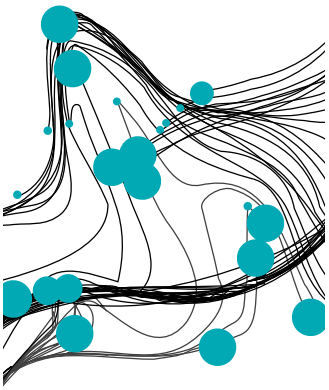

Engineering Technology (ET)

A study on the effect of local pressure gradient on turbulent boundary layer characteristics and trailing-edge noise over a flat plate.

A numerical and empirical study

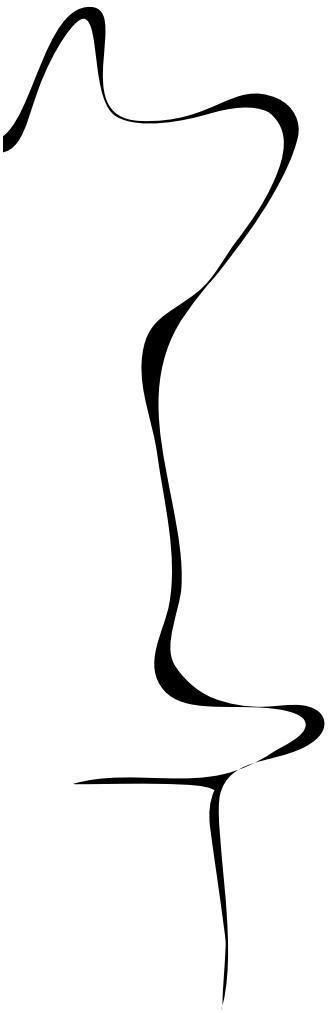

Mechanical Engineering, Faculty of Engineering Technology (ET)

Universiteit Twente
PO Box 217
Tel 053 489 9111
7500 AE Enschede

Thesis as part of the requirements for the title Master of Science

Author:	M.J.H. Vliem
Student number:	s1717707
Committee:	prof. dr. ir. C.H. Venner - Chairman
	dr. ir. M.J.P. Sanders - Daily supervisor
	dr. ir. L. Hirschberg
	dr. T. Zhu - External member
Publication date:	November 5, 2024
EFD document number:	461

UNIVERSITY OF TWENTE.

Abstract

Anthropogenic noise has become ever more prevalent since the industrial revolution and unfortunately, the transition to wind energy will only add to this problem. Noise contributions by wind turbines and air traffic are widely debated in Dutch politics. This is due to the big impact these political choices will have on the living environment of both humans and animals a solid understanding of these noise productions is desired. The field of aeroacoustics studies the domain where the noise is generated by a fluid instead of a vibrating solid. In contrast to many sound sources in these cases, it is not necessarily a solid that vibrates causing pressure fluctuations. In these cases, the fluid itself generates these fluctuations. Often the trailing edge noise mechanism is the most significant contributor to applications like wind turbines, aircraft and ships. This mechanism consists of an interaction between the unsteady flow in a turbulent boundary layer and a sharp trailing edge. Therefore the noise generated by this mechanism mainly depends on the boundary layer behaviour at this trailing edge. Amiet provided a model to describe the far-field noise spectrum (S_{pp}) with the turbulence statistics of the boundary layer and airfoil response, although these turbulence statistics are generally unavailable for most practical applications.

Amiet, solves the unavailability of these statistics by assuming a low Mach number, introducing the cross-correlation length ($l_y(\omega)$) and using several semi-empirical relations to only depend on a boundary layer integral parameter. Although available for flat plate scenarios, these relations become less valid as the equilibrium of the boundary layer is (locally) disturbed. Since this is the case for almost all real-world applications, PhD-candidate Ka-Kin Tou is attempting to develop a better understanding for the trailing edge noise generation in these (local) non-equilibrium turbulent boundary layers. This research assists by investigating how these boundary layers can be brought out of equilibrium without generating significant disturbances in the measurements of interest, implemented by two counter bodies at a limited angle of attack. This has occurred in two stages, firstly with computational fluid dynamics (CFD) simulations of the proposed set-up of Ka-Kin and secondly by validating these simulations in the aeroacoustic wind tunnel of the University of Twente. The CFD analysis was performed in the finite volume package `SU2`, using an incompressible configuration with the Spallart-Allmaras turbulence model, for a total 25 different configurations. The wind tunnel measurements consisted of pressure port measurements to quantify the effective equilibrium disturbance, hot-wire anemometry in order to determine boundary layer integral parameters and far-field microphone array measurements to determine if there is a distinct noise source measurable at the trailing edge.

The pressure calculated in CFD concurred with a quasi-one-dimensional calculation. The gradient was then taken and non-dimensionalized in the Rotta-Clauser parameter (β) which was found to be $\min(\beta) < -0.5$ and $\max(\beta) > 2.0$. Although the measured pressures show a similar trend, its magnitude was smaller. It is expected that this can be improved with the suggested measurement improvements. The boundary layer integral parameters were calculated for both the CFD data and the hot-wire anemometry velocity profile, but due to hardware complications, the amplitude of the latter was deemed unsound. However, since the amplitude is disregarded in the calculation of the parameters a comparison could still be made. For an alteration of the height between the counter body and the flat plate in the CFD results, the boundary layer thickness and shape parameter showed inverse trends, while showing proportional trends for alterations of the angle of attack in the counter bodies. It was only possible to make these results for the Hot-wire data after significant post-processing but although showing values close to those found with CFD, no trends were spotted. Finally, the acoustic data was analysed using a beamformer code and for all configurations, a clear noise source can be distinguished at the trailing edge in a frequency bin of $1500Hz < f < 2500Hz$. In these results, the counter bodies generate a larger trailing edge noise source but not so large that it makes the detection of the flat plate trailing edge noise source impossible.

Contents

1 Introduction

How noise can be mitigated is a more and more relevant question in modern society. From the view point of a Dutch person one is confronted with it on a daily basis. From people living in the rather busy area around Schiphol being annoyed by approaching aircraft or the people living one of our airbases enjoying the new (and increased) sound of the newly purchased F-35, to the people having strong opinions about wind turbines being build closely to their home. All of these noise mechanisms are covered by the field of acoustics and unfortunately for the people already seeing it as a nuisance, there is only a trend moving up in the applications mentioned before.

1.1 Anthropogenic noise

The production of noise by aerodynamic effects (aeroacoustics) is not a new phenomenon. The laws of nature are far older than mankind, so why has it become so relevant all of a sudden? Relative to the time mankind is roaming the planet, only in a very small portion it is consuming significant amounts of energy. The industrial revolution was a clear turning point in our way of living, from huge improvements in medicine to the establishing of universal human rights. However, in our quest for constant improvement, an ever-increasing consumption trend is strongly correlated. This consumption trend has been negatively impacting almost all species. This can be seen in our increased activity on the seas [38] impacting aquatic life and deforestation on land resulting in problematic migration[31]. As humans, we can largely blame ourselves for these effects, fixing these problems is one of the most important struggles of our generation. One of the solutions that can contribute, is new forms of energy such as wind energy. Unfortunately, as with many new technologies it is still often misunderstood by the general public and our self-centric mindset might enlarge our own threats to these new technologies while downplaying the benefits to the masses. As such, significant resistance against the placement of wind turbines occurs [40, 42], while the environmental benefits against other energy sources can not be understated [4]. This mistrust in wind energy is likely to be further enlarged by the already increasing levels of anthropogenic noise production connected to our ever-increasing consumption levels. A better understanding of the noise mechanisms might be a partial solution to this problem as it might offer a wider understanding to the general public and will likely offer opportunities in the mitigation of perceived anthropogenic noise.

1.2 Relevance to the energy transition

As the author is Dutch and is therefore mostly confronted with the Dutch ecosystem, the first alinea might give the impression that this is mainly a local issue but this could not be further from the truth. Across the academic and political spectrum it is widely agreed that there is a need for sustainability and since solar power can only be a part of this solution [11], wind energy is going to be of increasing influence on the global electricity production. Luckily, from a financial point of view wind turbines make a lot of sense even compared to most fossil fuels as shown in figure 1, safeguarding this route of the energy transition.

1.3 The Trailing-Edge Noise Mechanism

Sound from wind turbines is one of the prominent objections against the construction of new wind turbines and an improved understanding of the mechanisms behind the production of this sound is therefore paramount for successful further transition. Simultaneously outside the energy sector, there exists a significant motivation to improve the current understanding of noise generation models as shown by interest from the aviation industry and maritime sector.

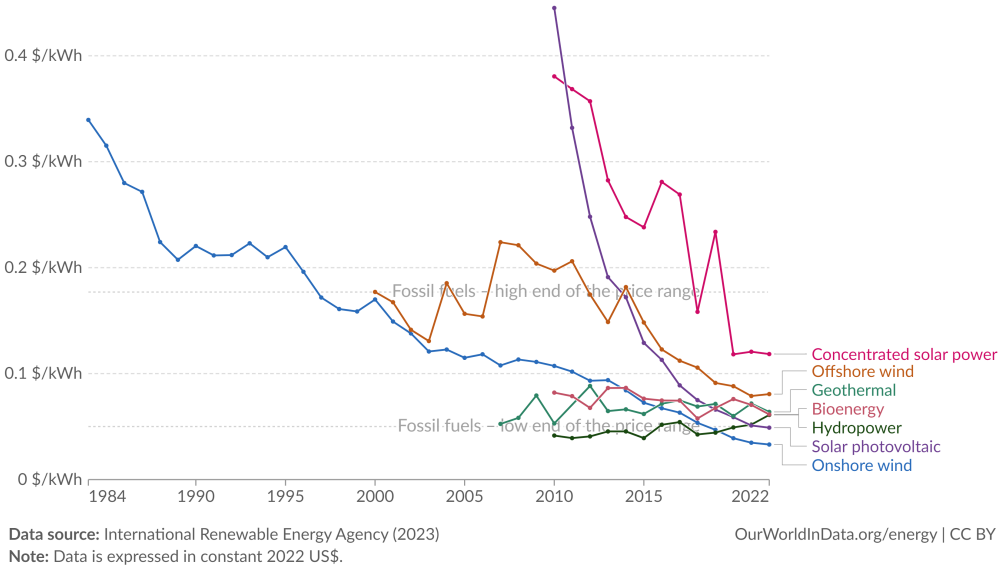

Figure 1: Levelized cost of energy by technology, World [29]

Although several research endeavours have attempted to model the noise emitted from airfoils [1][7][32] and as such tried to model one of the most significant contributions to these noise sources, this modelling is far from complete. Many of the current models use integral boundary layer parameters in single locations to predict their contribution to the overall noise generation but often assume flat plate-like behaviour concerning the creation of this boundary layer. This research tries to further the understanding of these noise sources under "non-standard" conditions.

2 Trailing-Edge Noise Prediction

Several noise production mechanisms can be identified in the aeroacoustic domain, so what should be the priority? Brooks et al. identified five mechanisms (shown in figure 2) where the flow itself causes the noise (self-noise). However, typical applied flow cases are not simple and the actual composition of these mechanisms might therefore not be trivial. It is for that reason that Oerlemans et al. researched the noise generated by wind turbines. This was done by applying the so called beam-former technique. It is able to visualize the position of sound in a similar fashion as modern radar systems determine the position of objects. Instead of a radar antenna, it uses a microphone array that in this case was placed on the ground (where humans would typically be hindered by the noise). Oerlemans et al. show that besides a small contribution on the hub, the noise production to the microphone array is dominated near the tip of the wind turbine blade while on the downstroke [30]. This technique is further explained in section 6.6. When comparing these findings with mechanisms identified by Brooks et al. the high directivity of hearing the downstroke especially and the concentration of noise production near the blade tip where the velocity is high are consistent with the trailing edge noise mechanism. This mechanism has proven to be dominant in these kind of flow regimes [30] and therefore warrants further research.

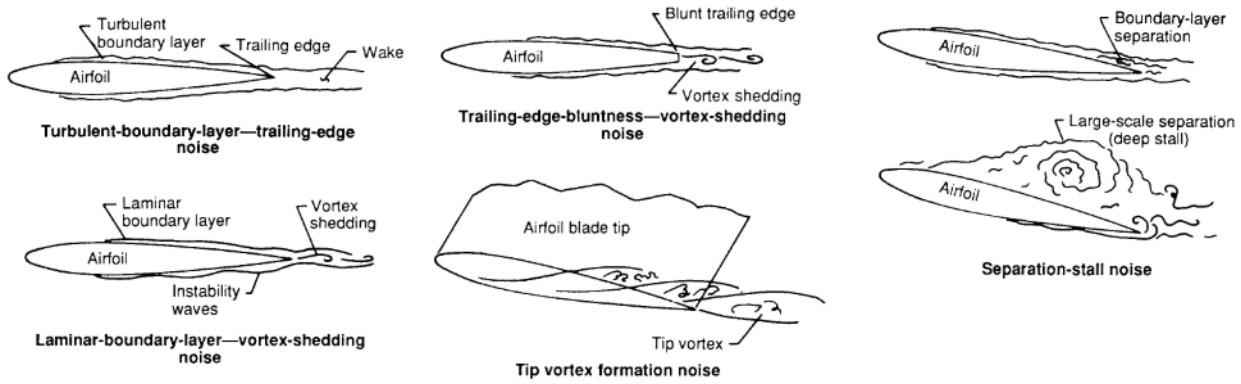

Figure 2: Flow conditions producing airfoil blade self-noise [7]

2.1 Amiet's Trailing-Edge Noise Model

Modelling aeroacoustic noise is relatively new and therefore investigating the assumptions behind these models is of extra interest. The easiest way to understand these core assumptions is by reviewing how such a model came to be. The model of focus in this study is Amiet's trailing edge noise model, which sees the trailing edge noise as a quadrupole distribution along the trailing edge. However, it is expected that a dipole contribution will actually be dominant for most low Mach numbers. Looking more fundamentally at what Amiet tries to describe with these sources, the unsteady loading due to the pressure fluctuations in two boundary layers is regarded. Amiet therefore focuses on a flat plate where the contribution on both sides should act statistically equal, assuming that it is only necessary to obtain an expression for these pressure fluctuations on one side. To obtain an actual expression for the far-field noise spectrum (S_{pp}) Amiet starts with Curle's equation [12], which is in its turn a formal solution to the Lighthill analogy taking hard surfaces into account. An example of this derivation is provided by Devenport and Glegg[13] and is therefore not included in this report. The derivation assumes that the trailing edge does not create new disturbances and that both a non-penetration and a Kutta condition apply. The product of this derivation is equation 1 where the blue term represents the turbulence statistics mentioned before, the red term represents the airfoil response and the remaining terms represent the noise statistics. Such a clear distinction is made because Amiet suggests that the pressure fluctuation can be split into an undisturbed boundary layer contribution and a fluctuation response at the trailing edge.

$$S_{pp}(\vec{x},\omega) = \left(\frac{\rho k z b}{\sigma_0^2}\right) \pi U d \Phi_{ww}(K_x, K_y) |\mathcal{L}(\vec{x}, K_x, K_y)|^2 \tag{1}$$

$$S_{pp}(x,0,z,\omega) = \left(\frac{\omega z \rho_0 b M}{\sigma_0^2}\right) d |\mathcal{L}(x, K_x, 0)|^2 l_y(\omega) S_{ww}(\omega) \tag{2}$$

Although giving a general description of the far-field noise, the usability of equation 1 is still rather limited. This is mainly due to the fact that the turbulence statistics will be unknown in many practical cases. In these cases just measuring these statistics is highly impractical and therefore further simplification is desirable. As such, the case of an observer in the plane $y = 0$ is analysed, where only the $k_y = 0$ gusts contribute to the emitted sound. However, Amiet mentions that in the $y \neq 0$ cases the k_y term can be replaced with $\omega y / c_0 \sigma$ as long as the axial Mach number remains small[1]. Consequently Amiet uses Graham's similarity rule to show an independency of k_y for Φ_{ww} and $\mathcal{L}$ when the parameter $\Lambda \equiv M K_x d$ becomes large. Combined with the introduction of the cross-correlation length $l_y(\omega)$ Amiet is able to rewrite equation 1 to 2.

2.2 Semi-Empirical Modelling

The amount of well-documented scenarios for airfoil surface pressure characteristics is minimal, with Amiet stating in 1975 that it is limited to the equilibrium boundary layer. In that case Corcos represents the normalized cross-spectrum ($S(\omega, y)/S(\omega, 0)$) by the function $B(\omega y / U_c)$[10], which only depends on a single dimensionless variable. Amiet then integrates this function to result in equation 3. Then also for the surface pressure spectrum, an empirical relation can be used. The one from equation 4 by Willmarth and Roos is reported to approximate the surface pressure spectrum for a turbulent boundary layer with density ρ_0 and free stream speed U [45] where $\tilde{\omega} = \omega \delta^* / U$ and $0.1 < \tilde{\omega} < 20$. Next an expression for U_c is needed, however, this convection velocity contains some small variations that are still unknown. In order to still have an expression, the variations will be ignored and an average value ($U_c = 0.8U$) is used. Finally, the turbulent boundary layer displacement thickness (δ^*) is approximated as a function of the chord-based Reynolds number in equation 5 [18].

$$l_y(\omega) \approx 2.1 \frac{U_c}{\omega} \tag{3}$$

$$S_{pp}(\omega, 0) = \frac{(\frac{1}{2}\rho_0 U^2)^2 (\delta^*/U) 2 * 10^{-5}}{1 + \omega + \tilde{0}.217\tilde{\omega}^2 + 0.00562\tilde{\omega}^4} \tag{4}$$

$$\delta^* \approx 0.047 c Re_c^{-0.2} \tag{5}$$

Together with an expression for the airfoil response ($|\mathcal{L}|$) that Amiet presents [1] as valid for any turbulent flow case past a trailing edge for which the assumption of stationary turbulence is reasonably supported. This closes the set of equations and makes it possible to give a prediction of the far-field noise. The cases for which this prediction is applicable are, however, extremely limited. This is mostly due to the large amount of empirical relations mentioned before that are all of limited validity. This makes accurate and widely applicable application of equation 2 dependent on empirical data with regard to the pressure statistics of the turbulent boundary layer. This unfortunately still requires a significant number of measurements.

3 Wall-Bounded Flows

Due to the no-slip condition in boundary layers, the flow velocity at the bottom of a boundary layer has to be zero and thus the boundary layer is the transition from the free stream velocity v_∞ to a zero velocity. In slowing down the mass of the flow due to shear stress an arm is created and thus a moment on the flow is enacted. The ratio between the creation of these moments and their dampening (presentent in the Reynolds number), the difference in speed, any pressure gradients and a lot of other influences all dictate the properties of the boundary layer. As it is the interface between the flow and any object we can place in it, its structures and properties are most fascinating in comprehending the field of aerodynamics.

As the flow already satisfies the no-slip condition in the stagnation point, it is logically the point from which the boundary layer grows. Eventually, the arm of the moment applied to the fluid can become dominant and then transition from a laminar to a turbulent boundary layer can occur. This then impacts the velocity profile of the boundary layer and as such, the forces that are enacted through this interface. An overview by Drela of a typical boundary layer is given in figure 3.

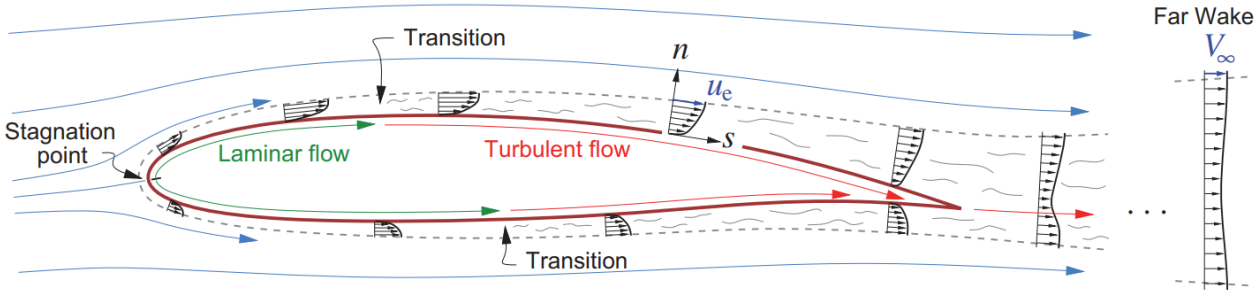

Figure 3: Boundary layer and wake development on a typical airfoil, shown by the $u(n)$ velocity profiles. The layer thicknesses are shown exaggerated [17].

3.1 Governing Equations

In the construction of a set of governing equations for the turbulent boundary layer, the full Navier-Stokes momentum equation is a good starting point, as it will encompass all the force components described in the preceding paragraphs. As shown in equation 6 it is however an impractical large set of equations and it can be somewhat reduced by applying the Thin Shear Layer (TSL) approximations. These approximations state that the parallel velocity is dominant over the normal velocity ($v \ll u$), the parallel velocity gradient with respect to normal direction is dominant over that with respect to the parallel direction ($\partial u/\partial s \ll \partial u/\partial n$) and that there is no relevant pressure gradient with respect to the normal direction ($\partial p/\partial n \simeq 0$). These assumptions reduce the 2D shear stress tensor ($\bar{\bar{\tau}}$ to an off-diagonal tensor only containing the component τ. It also reduces the n-momentum equations to the inviscid flow edge pressure which is constant along n (synonymous with y^*[1]). As a result, the streamwise pressure gradient in the remaining s-moment equation is to be replaced with the edge velocity gradient as shown in equation 7.

$$\rho\frac{D\vec{V}}{Dt} \equiv \rho\frac{\partial\vec{V}}{\partial t} + \rho\vec{V}\cdot\nabla\vec{V} = \rho\vec{f} - \nabla p + \nabla\cdot\bar{\bar{\tau}} \tag{6}$$

$$-\frac{\partial p}{\partial s} = -\frac{dp_e}{ds} = \rho_e u_e\frac{\partial u_e}{\partial s} + \rho_e v_e\frac{\partial u_e}{\partial n} \simeq \rho_e u_e\frac{du_e}{ds} \tag{7}$$

[1]It should be noted that while Drela uses the variable n to indicate the normal direction from the surface through the boundary layer, it is typically associated with any normal direction. This thesis, therefore prefers the use of the term y^* also indicating the normal distance to the non-penetration condition, through the boundary layer.

Applying these assumptions on equation 6, results in equations 8, 9 and 10. In equation 10 the effective viscosity (μ) is actually the sum of the dynamic component and term representing the turbulence as presented in equation 32 and explained in section 4.2. An absence of this turbulence expression leaves the set of governing equations open and is referred to as the closure problem.

$$\frac{\partial(\rho u)}{\partial s} + \frac{\partial(\rho v)}{\partial n} = 0 \tag{8}$$

$$\rho u \frac{\partial u}{\partial s} + \rho v \frac{\partial u}{\partial n} = \rho_e u_e \frac{du_e}{ds} + \frac{\partial \tau}{\partial n} \tag{9}$$

$$\tau = \mu \frac{\partial u}{\partial n} \tag{10}$$

As mentioned before, the boundary layers form as a result of the no-slip condition, but what if the viscosity causing this no-slip condition is neglected? In that case, the free stream velocity would extend all the way up to the surface. Comparing this inviscid case with the real viscous case there exists a mass deficit that is visualized by Drela in figure 4.

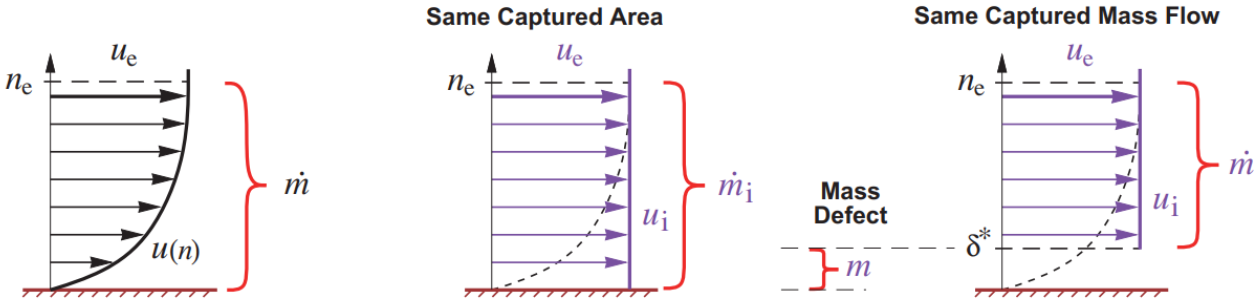

Figure 4: Comparison of actual and Equivalent Inviscid Flow (EIF) mass flows [17].

A keen observer might already have deduced that the mass deficit illustrated in figure 4 is equal to the area between the dotted line ($u(n)$) and the right solid line ($u_1 = u_e \equiv u_\infty$), since it represents the extra mass that would flow through the control volume when neglecting the viscosity. This means that this mass defect (Δm) is expressible in the integral form of equation 11. As the inviscid control volume achieves the same mass throughput while being smaller, there exists a volume decrease where it exactly matches the full viscous control volume. This volume has a height of the original control volume height (n_e) minus a correction displacement (δ^*). This mass displacement thickness can then be used in wall displacement models to mimic viscous simulations while solving the simpler inviscid case where the boundaries are displaced by the mass displacement thickness. This principle is the basis for panel methods such as XFOIL by Drela.

$$\Delta m = \int_0^{n_e} (\rho_e u_e - \rho u) dn = \rho_e u_e \delta^* \tag{11}$$

The same principle can be applied to the momentum and kinetic energy flowing through the control volume, resulting in the momentum and kinetic energy deficits (P equation 12 and K equation 13 respectively). A momentum displacement (θ) and kinetic energy displacement (θ^*) can be be extracted the create the set δ^*, θ and θ^* which are referred to as the integral boundary layer parameters. Under an incompressibility assumption, Drela reduces these to equations 14, 15 and 16 respectively, where $U = u/u_e$. Since these integral parameters express different orders of the velocity profile, a combination of these parameters is analogous for the shape of the velocity profile and due to the fact that they all have meters as their dimension, a division of these integral parameters results in the dimensionless shape parameter H (equation 17) and kinetic shape parameter H^* (equation 18).

$$P = \int_0^{n_e} (u_e - u)\rho u dn = \rho_e u_e^2 \theta \tag{12}$$

$$K = \int_0^{n_e} (u_e^2 - u^2)\rho u dn = \rho_e u_e^3 \theta^* \tag{13}$$

$$\delta^* = \int_0^{n_e} (1 - U) dn \tag{14}$$

$$\theta = \int_0^{n_e} (U - U^2) dn \tag{15}$$

$$\theta^* = \int_0^{n_e} (U - U^3) dn \tag{16}$$

$$H \equiv \frac{\delta^*}{\theta} \tag{17}$$

$$H^* \equiv \frac{\theta^*}{\theta} \tag{18}$$

3.2 Equilibrium and Non-Equilibrium Turbulent Boundary-Layers

For most boundary-layers in equilibrium, the characteristic properties are simply a scaled version of themselves along this equilibrium, and in that sense, they do not contain any historical effects. Since boundary layers tend to move to equilibrium eventually, they will then contain a local β and Re value but contain the historical effects. Therefore, depending on its non-equilibrium upstream history, even an equilibrium boundary layer at the trailing edge can be highly interesting. Of course, a local pressure gradient is not the only source disturbing a potential equilibrium condition, similar behaviour can also be caused by surface roughness and changing geometry.

3.2.1 Non-Zero Pressure Gradient Boundary-Layers

To analyse the effect of pressure gradients on the boundary layer, Drela, temporarily redefines s as the distance along a streamline and n as the distance perpendicular to it, then logically $v = 0$ and the s-momentum equation can be approximated using equation 19. This description containing the velocity can be expressed over a small distance along the streamline (Δs) to extract a velocity increment in equation 20.

$$\rho u \frac{\partial u}{\partial s} = \rho_e u_e \frac{du_e}{ds} + \frac{\partial \tau}{\partial n} \tag{19}$$

$$\Delta u \approx \frac{\partial u}{\partial s}\Delta s = \frac{\rho_e u_e}{\rho u}\Delta u_e + \frac{1}{\rho u}\frac{\partial \tau}{\partial n}\Delta s \tag{20}$$

Drela states that the first term in equation 20 represents the spatial derivative of the pressure along the streamline (dp/ds). Suppose that the pressure gradient is negative ($dp/ds < 0$), it is classified as a *favourable pressure gradient* and as expected for a subsonic flow this corresponds to an *accelerating boundary layer*. As the gradient is applied regardless of the normal direction, the volumetric acceleration is also independent of the normal distance. However due to the $\frac{\rho_e u_e}{\rho u}$ term of equation 20, the slower element responds stronger. This results in the lower part of the velocity profile extending more than the top part and as such, results in an overall more rectangular profile as Drela illustrates in figure 5. The opposite case is a positive pressure gradient ($dp/ds > 0$). This positive gradient is referred to as the *adverse pressure gradient* as it relates to a decelerating flow that has a lower tendency to stay attached (the same reasoning applies to the negative/favourable gradient).

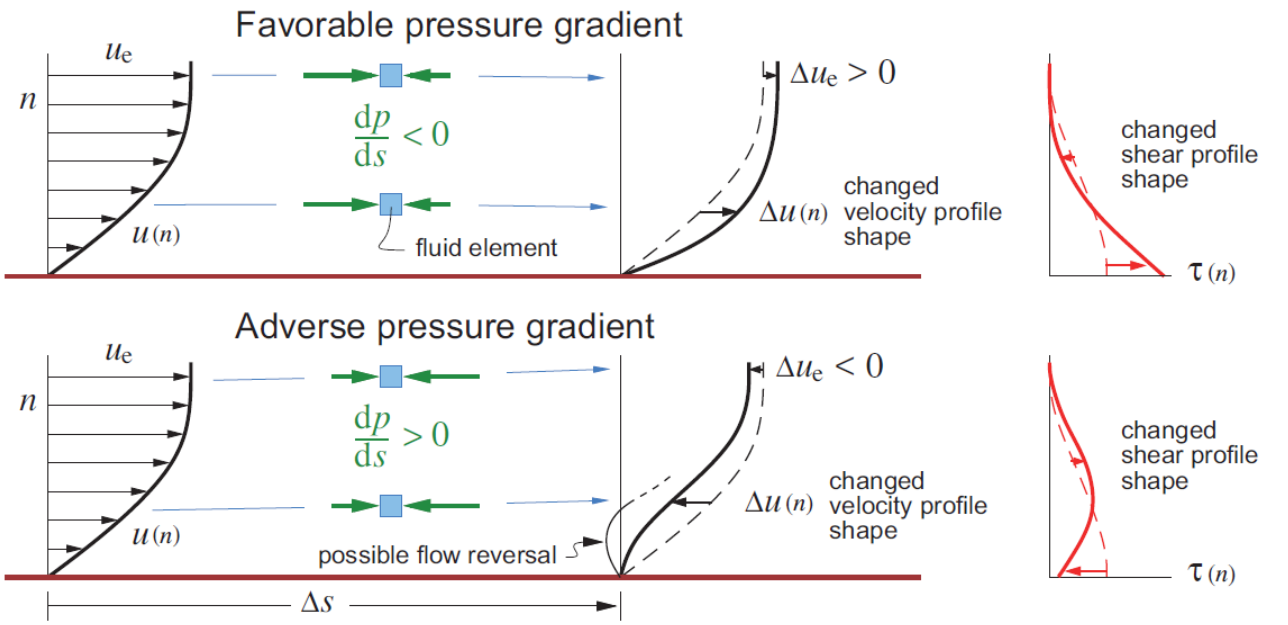

Figure 5: Velocity changes Δu along streamlines resulting from a favourable or adverse pressure gradient which applies the same accelerating or decelerating net force per unit volume to all fluid elements. Slower-moving elements have a larger Δu, resulting in a distortion of the velocity profile. A sufficiently strong adverse pressure gradient will cause a flow reversal and boundary layer separation. [17]

This pressure gradient can be non-dimensionalized (equation 21) using the boundary layer displacement thickness and the wall shear stress, as first suggested by Clauser[9]. The non-dimensionalized parameter β is then proportional to a normal pressure expression ($\delta^* dp/dx$) over the shear stress (τ_w) as shown in momentum integral equation 22. Intuitively one might expect this parameter to be constant, as it is an important requirement for the boundary layer to be in equilibrium, but Devenport and Lowe note that its dependence on the inner and outer parameters makes developing boundary layers exempted from this initial reasoning.

$$\beta = \frac{\delta^*}{\tau_w}\frac{\partial p}{\partial x} \tag{21}$$

$$\frac{d}{dx}(\rho u_e^2 \theta) = \tau_w + \delta^* \frac{dp_e}{dx} \tag{22}$$

3.3 Relevance To Trailing-Edge Noise

Although the zero pressure gradient boundary layer is thoroughly studied, most real-world applications consist of either adverse or favourable local pressure gradients. This is by definition the case for airfoils, for which its effectiveness is a direct function of its ability to create a pressure difference between its pressure and suction side. Even in the relatively simple symmetric airfoils, these pressure gradients occur, due to the acceleration of the flow over the thicker section of the airfoil. These and other causes of local non-equilibrium conditions influence the history effects of the turbulent boundary layer as mentioned in the previous paragraphs and contribute to the turbulence statistics part of equation 1. Being able to mimic the boundary layer properties of these common airfoils will allow for the study of its aeroacoustic effects in a controlled environment. As studies into these aeroacoustic effects are well underway, it is relevant to study the achievability of the generation of these boundary layers in a cost-effective and systematic framework.

3.3.1 Typical Non-Dimensional Pressure Gradients

Using panel method solvers such as Drela's `XFoil`, can provide a good estimation of pressure distributions in a time-effective manner. For a NACA0018 and NACA4412 this results in the pressure coefficient distribution of figure 6a. As is evident from these slopes, the gradient is almost ever-changing and coupled with the transition behaviour indicated by the laminar separation bubble bumps, it can be deduced that these boundary layers are subjected to many non-equilibrium effects. In the case of the NACA 4412 a numerical simulation was performed by Vinuesa et al. and its boundary layer was evaluated at equal conditions as the XFoil results of figure 6a. Vinuesa et al. report relevant β parameters to be 0.6 at $x/c = 0.4$ and 14.1 at $x/c = 0.9$ as shown in tables 1 and 2.

Table 1: Boundary-layer parameters at $x/c = 0.4$ [41]

Parameter	Suction side	ZPG DNS	Pressure side
Re_τ	242	252	174
β	0.6	$\simeq 0$	-0.12
Re_θ	712	678	407
H	1.59	1.47	1.59
C_f	$4.1 * 10^{-3}$	$4.8 * 10^{-3}$	$5.5 * 10^{-3}$
κ	0.38	0.42	0.41
B	4.20	5.09	4.63
$\sqcap$	0.56	0.31	0.41

Table 2: Boundary-layer parameters at $x/c = 0.9$ [41]

Parameter	Suction side	ZPG DNS	Pressure side
Re_τ	328	359	317
β	14.1	$\simeq 0$	-0.16
Re_θ	2.255	1.007	785
H	2.03	1.45	1.48
C_f	$1.2 * 10^{-3}$	$4.3 * 10^{-3}$	$4.6 * 10^{-3}$
κ	0.23	0.41	0.42
B	-2.12	4.87	5.17
$\sqcap$	1.83	0.37	0.3

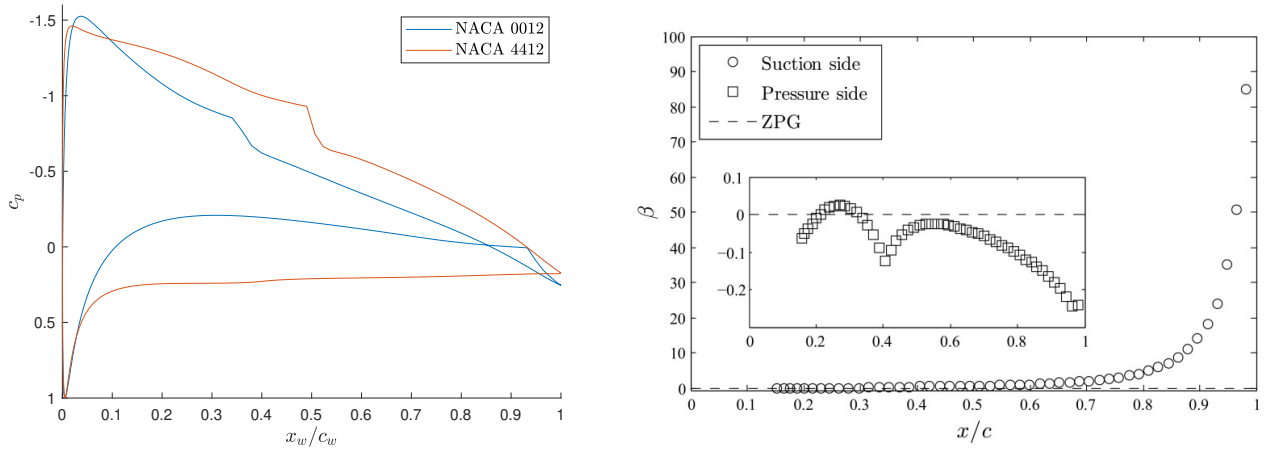

(a) Pressure coefficient at $\alpha = 5°$ and $Re = 4 * 10^5$

(b) β at $\alpha = 5°$ and $Re = 4 * 10^5$[41]

Figure 6: Typical pressure (gradient) for common airfoils

4 Numerical Approach

Ideally, wind tunnel experiments would always be fast, cheap, and without any measurement error. Unfortunately, this is not yet the case, but as long as numerical simulations can properly be validated the number of empirical measurements can be limited.

4.1 Reynolds Averaged Navier-Stokes (RANS)

Reynolds averaged Navier-Stokes or RANS is something often referred to in the domain of computational fluid dynamics and since it is also used in these simulations, it warrants an introduction.

4.1.1 Navier-Stokes equations

While purists would state that the Navier-Stokes equations only contain three equations describing the balance of momentum (assuming three dimensions are modelled), in most applications (including examples of the Glenn Research Centre[22] and in teaching [24]), it refers to five equations that in addition to the momentum in three directions also describe the mass balance and energy balance. Their general form is that of equation 23 and it is intuitively best understood when applied to a control volume. When regarding this control volume the term $\nabla \cdot \vec{F}^c(V) - \nabla \vec{F}^v(V, \nabla V)$ represents the amount of parameter V flowing over its boundaries, S represents the generation and/or destruction of that same property in the control volume and thus $\frac{\partial V}{\partial t}$ represents the accumulation of that property in the control volume. In short, it is the balance that states that everything that is flowing in minus everything that is flowing out plus everything that is generated as to be equal to the accumulation of that property in the volume. In theory, when done correctly, this bookkeeping would result in zero. However, in many iterative schemes, a guess is used for every property and how close the equations become to zero is then a measure of the quality of the guess. These values are indicated with $R(V)$ and are named *residuals*, which can be seen as part of the numerical error still present in the current guess. Although this now provides a set of equations to model all fluid flows regarding a control volume, a more general form is applicable regardless of that volume. This is obtained by dividing by the volume thus formatting all terms in a density form. The in- and out-flow will then become flux terms, the accumulation term will become a density rate and the source term a volumetric source.

$$R(V) = \frac{\partial V}{\partial t} + \nabla \cdot \vec{F}^c(V) - \nabla \vec{F}^v(V, \nabla V) - S = 0 \tag{23}$$

4.1.2 Governing Equations for low Mach numbers

In the case of the Navier-Stokes equations, the quantities to be conserved are mass-, momentum- and energy density. These quantities expressed with U are given in equation 24, but since the range of Mach numbers is expected to be relatively low, the flow can be regarded as incompressible and as such, a set of working variables (V) replace these conservative variables as expressed in equation 25. In its incompressible setting SU2 does, however, not set a constant density but rather applies the low-Mach/incompressible ideal gas formulation [19]. This approach allows for the expansion and contraction of the fluid as a result of thermal in- and out-put.

$$U = \begin{Bmatrix} \rho & \rho\vec{v} & \rho c_p T \end{Bmatrix}^T \tag{24}$$

$$V = \begin{Bmatrix} p & \vec{v} & T \end{Bmatrix}^T \tag{25}$$

In modeling the flux term $\nabla \cdot \vec{F}^c(V) - \nabla \vec{F}^v(V, \nabla V)$ a distinction can be made between the convective $(\nabla \cdot \vec{F}^c(V))$ and viscous contribution $(\nabla \vec{F}^v(V, \nabla V))$, with $\vec{F}^c$ being expressed in equation 26 and $\vec{F}^v$ being expressed in equation 27. In these equations, $\vec{v}$ is the Cartesian velocity vector, p is the pressure, $\underline{\tau}$ is the viscous stress tensor, T is the temperature and κ is the thermal conductivity. This requires three additional expressions: the first for the density in equation 28, the second for the viscous stress tensor in equation 29 and the third is an expression of the viscosity for which Sutherland's law can be applied to close the set of equations.

$$\vec{F}^c = \begin{Bmatrix} \rho\vec{v} \\ \rho\vec{v} \times \vec{v} + \underline{I}p \\ \rho E\vec{v} + p\vec{v} \end{Bmatrix} \tag{26}$$

$$\vec{F}^v = \begin{Bmatrix} \cdot \\ \underline{\tau} \\ \underline{\tau} \cdot \vec{v} + \kappa \nabla T \end{Bmatrix} \tag{27}$$

$$\rho = \frac{p_0}{RT} \tag{28}$$

$$\underline{\tau} = \mu(\nabla\vec{v} + \nabla\vec{v}^T) - \mu\frac{2}{3}\underline{I}(\nabla \cdot \vec{v}) \tag{29}$$

4.1.3 Reynolds averaging

As turbulence occurs on very small time scales, calculating a solution becomes extremely expensive across the entire range of time scales. Reynolds, therefore suggested splitting the velocity into a time-averaged term $(\bar{u}_i)$ and a fluctuating term (u_i'), resulting in equation 30 with the condition of equation 31. The contribution of the fluctuation term to the total stress tensor can be isolated and is referred to as the Reynolds stress. While this term allows for the inclusion of turbulent flows in the equations established before, maintaining computational viability, it does add a term to the closed set of equations. This creates the *closure problem* and unfortunately, it is highly non-linear.

$$u_i = \bar{u}_i + u_i' \tag{30}$$

$$\bar{u_i'} = 0 \tag{31}$$

4.2 Turbulence Model For The Closure Problem

One of the first to solve the closure problem was Boussinesq who categorizes two contributions in the viscosity. The first of these is the dynamic component that was already incorporated in paragraph 4.1.2 and the second is a turbulence component. This results in equation 32 for the effective viscosity and it has been the basis for the linear eddy viscosity models [35]. This also applies to the thermal conductivity which can now be expressed using equation 33.

$$\mu = \mu_d + \mu_t \tag{32}$$

$$\kappa = \frac{\mu_d c_p}{Pr_d} + \frac{\mu_t c_p}{Pr_t} \tag{33}$$

4.2.1 The Spalart-Allmaras Model

One of the simpler models for closing the set of equations is the model by Spalart and Allmaras, where just a single additional equation is used that describes the transport of a viscosity variable. This transport equation (equation 34) is fundamentally very similar to equation 23, but the variable needs a transfer function for μ_t to be useful in the current set of governing equations. This function is given by equation 35.

$$\frac{\partial \tilde{\nu}}{\partial t} + u_j \frac{\partial \tilde{\nu}}{\partial x_j} = c_{b1}(1 - f_{t2})\tilde{S}\tilde{\nu} - \left(c_{w1} f_w - \frac{c_{b1}}{\kappa^2} f_{t2}\right)\left(\frac{\tilde{\nu}}{d}\right)^2 + \frac{1}{\sigma}\left(\frac{\partial}{\partial x_j}\left((\nu + \tilde{\nu})\frac{\partial \tilde{\nu}}{\partial x_j}\right) + c_{b2}\frac{\partial \tilde{\nu}}{\partial x_i}\frac{\partial \tilde{\nu}}{\partial x_i}\right) \tag{34}$$

$$\mu_t = \rho\tilde{\nu}\frac{(\frac{\tilde{\nu}}{\nu})^3}{(\frac{\tilde{\nu}}{\nu})^3 + c_{v1}^3} \tag{35}$$

From the transport equation above, the keen reader might already deduce that the turbulence is not significantly dissipated in this model and it should be mentioned that the original authors of the model already predicted the misuse of their and many other turbulence models as transition prediction models, while warning for their unsuitability in these roles. This causes virtually the entire boundary layer on the test set-up of section 6 to be turbulent as can be seen from figure 7, where the boundary layer shape parameter is plotted in the flat plate section. Here, the shape parameter is immediately between 1.2 and 1.6 supporting the assumption of immediate turbulent dominant effects in the boundary layer velocity profile. By causing the flow to be tripped, this inaccuracy can be significantly mitigated.

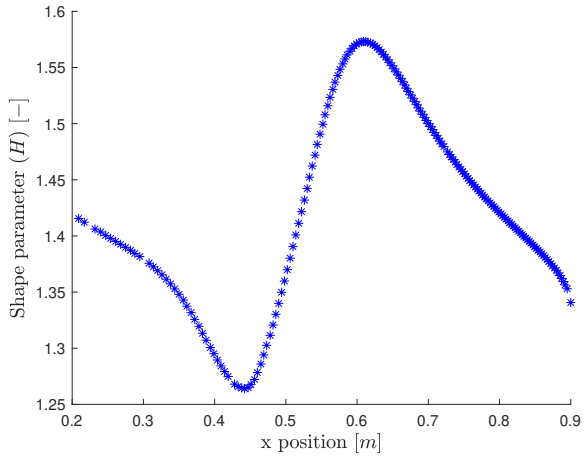

Figure 7: Boundary layer shape parameter $H_{1,2}$ distribution along the flat plate section of configuration 17 (table 3), showing $1.2 \leq H \leq 1.6$ and thus well within the domain of typical turbulent boundary layers.

4.3 Finite volume solvers

`SU2` and many other solvers of the Navier-Stokes equation set are finite volume solvers. Several other methods such as finite difference, spectral- and lattice gas/Boltzmann -methods exist, but it is expected that 80% of CFD implementations use finite volume methods[3]. This is mainly due to the lack of cell shape limitations, computational speed and memory efficiency for larger problems such as high speed-, turbulent flows and source-term-dominated problems.

As mentioned before, the finite volume solver balances a certain conserved variable within a control volume. This can, for example, be the momentum in a cell, where momentum can flow in over the cell faces (flux term), be accumulated in the cell (accumulation/time dependent term) and be created (source terms). It can be seen as a sort of accountancy for conserved variables[2], with mass momentum and energy instead of money. The imbalance in this bookkeeping is the aforementioned residual and since it is a measure of the solution quality (a zero term would indicate a perfect adherence to the governing equations), it is often monitored regarding iterative progress.

[2]Although it is more correct to refer to the five governing equations as balance equations rather than conservation equations, its main variables are still generally referred to as conserved variables.

Many settings influence the speed, stability and accuracy of the finite volume method, such as the numerical schemes, for which an understanding of its working principle is required. In order to achieve this understanding quickly, as an example, the one-dimensional linear advection can be regarded, as it only has a single conserved variable and a single governing equation, given in equation 36. This equation is already in the characteristic form of equation 37, enabling the identification of flux function f. This should be a function of the conserved variable and for this case is $f(\rho) = \rho$. This function has to be solved on the faces of each cell and therefore, the value at the cell face itself is needed. The numerical schemes obtaining this value all use some form of interpolation using the cell node values. This interpolation originates in a Taylor expansion on the cell face (half-node). This means that the truncation of the Taylor expansion determines the order of the scheme and thus its ability to accurately represent that order of behaviour in the calculation. The most intuitive way this becomes visible is by considering the first-order scheme, where the Taylor expansion is truncated as soon as possible, resulting in only looking at a constant value (if it is regarding a so-called upwind scheme, then the upwind value). So at cell face $n + 1/2$ (the downstream cell face of cell n) this would be $f(\rho_{n+1/2}) = \rho_n$. This is very stable but often results in added diffusivity, especially when the gradient is relatively large and thus, the first-order approximation is far off. In trying to resolve this effect, a central difference scheme can be used. In this scheme, an extra term is included in the Taylor expansion resulting in a linear interpolation. This linear interpolation means the averaging of the two cell values (assuming equal spacing) and thus $f(\rho_{n+1/2}) = 0.5(\rho_n + \rho_{n+1})$. This scheme can improve the accuracy significantly but may result in overpredictions, visible as oscillations in the solution and eventually even divergence. This can be mitigated by locally switching to a lower-order scheme, making this adaptation a hybrid scheme. Higher-order schemes and alternative interpolations such as a power-law scheme are also available, but it is typically advised to start with the simplest and most stable set-up [3] and increase the complexity where desired and possible. As upwind schemes are preferable in the convective terms of the Navier-Stokes equations [26] and the only available incompressible scheme in `SU2` is the flux difference splitting scheme, it is selected for the convective term. Meanwhile, the scalar upwind scheme is selected for the turbulence term as it is the most stable. Even under these stable conditions enabling the MUSCL schemes for this term resulted in significant instability leaving it only enabled for the convective term. This setting resulted consistently in converging behaviour.

$$0 = \frac{\partial \rho}{\partial t} + \frac{\partial \rho}{\partial x} \tag{36}$$

$$0 = \frac{\partial q}{\partial t} + \frac{\partial f(q)}{\partial x} \tag{37}$$

$$C = \frac{u \Delta t}{\Delta x} \tag{38}$$

Next to the spatial schemes, time integration also has a big effect on stability and computational speed. Although the simulation is steady state and thus the time is constant, the next iteration is computed in a mathematically similar fashion as the next step in time would be calculated. This iterative process is referred to as the *inner iteration*, while a time step would result in a new *outer iteration*. The size of this time step (Δt) can be given as an absolute value. However, it makes more sense to regard this value normalized by the spatial step (Δx) and the local velocity (u) into the Courant-Friedrichs-Lewy (CFL) number as given in equation 38. It represents the travel of information through the grid over the spatial and time discretization that has to capture it. A high CFL number typically results in a faster but less stable scheme and this is why many solvers contain an adaptive CFL parameter. This allows the relative unstable start (earlier iterations) to be under more stable conditions and then to ramp up to higher values when possible (reducing the overall number of iterations and computing time). This option was however kept disabled as the simulations showed divergent behaviour when enabling this option even at later iterations. The condition $CFL = 4.0$ did result in reliable convergent behaviour for all configurations and since computations were performed parallel the time gained with regards to run time was deemed to be insufficient compared to the time investment of further CFL optimization. As such the run time of the complete simulation would be in the ballpark of 28 hours when performed on the `TFE2` HPC cluster.

5 Numerical Simulations of a Flat Plate with a Locally Varying Pressure Gradient

PhD candidate Ka-Kin is currently investigating the trailing edge noise generation on a flat plate and as such investigating the effective generation of non-equilibrium boundary layers on his set-up was deemed to be most beneficial to scientific research.

5.1 The Problem Description

The goal of the set-up is to closely mimic the theoretical flat plate scenario while making as few concessions as possible when incorporating measurement devices. Special care has been taken by Ka-Kin in designing the leading and trailing edges so as to minimally impact the boundary layer. The flat plate with a chord length of $L = 1m$ consists for the first 15% out of a modified super ellipse, reaching a plate thickness of 1.2% chord length. This thickness is then maintained in a flat section until 90% chord length where a symmetric NACA profile forms the trailing edge. From the NACA profile only the last 70% will be used resulting in a continuous line from leading to trailing edge. A small airfoil of 20% plate chord length is then added to both sides halfway along the flat plate to create the desired pressure gradients.

5.1.1 Mesh Generation

Starting with the geometry defined in section 5.1, a discretization of the fluid domain has to be created to evaluate the Reynolds averaged Navier-Stokes equations of section 4 on. This can be achieved in both a structured and unstructured fashion, where the former typically outperforms the latter in computational work, but only the latter is capable of guaranteeing proper mesh quality in non-uniform geometries. As such, both types are utilized in different regions of the domain. On areas where flow behavior might be complex or its result deemed important such as the boundary layers and wakes, structured meshes are applied, while the rest of the domain is filled with unstructured mesh. As the unstructured part is the most adaptive, it will be added last.

Meshing always first occurs one-dimensional before this is used as seeding for the two-dimensional meshing. As this occurs at the domain edges, a discretization has to be set there first. On one hand, this is majorly influenced by the desired mesh resolution, but on the other hand, it also influences the cell geometry and as such, the local mesh quality. For this mesh quality to be high the cells should ideally have low skewness, cell size changes gradually and aspect ratios close to one [3]. Because of this desire to obtain ideal cells, the cell size can loosely be based on the desired cell height.

This cell height is in turn dependent on catching all flow phenomena of interest. As Kármán stated the inner layer of the boundary layer can be divided into three regions: First, the viscous sub-layer where all flow behaviour is relatively linear, then through a buffer layer to a log-law region where the velocity profile follows a logarithmic function of the normal distance to the wall. This first layer also has to be captured but it is relatively small and thus determines the initial cell height. This cell height and corresponding velocity are often expressed dimensionless in y^+ (equation 39) and u^+ (equation 40), to be applicable to a wide range of boundary layer cases. It is then common procedure to aim for $y^+ = 1$ as the target height for the initial cell height to be sure to capture the viscous sub-layer properly [3]. Although this value can be estimated using a flat plate analogy, as a rule of thumb an initial height of $y_0 = 10^{-6}m$ is often attempted in an initial CFD run to which the definite mesh is then adapted to. In the case of this thesis, this resulted in an increase by a factor of four ($y_0 = 4 * 10^{-6}m$) and was checked consequently as the y^+ value is not constant across the domain edge.

$$y^+ = \frac{y\sqrt{\tau_w/\rho}}{\nu} \tag{39}$$

$$u^+ = \frac{u}{\sqrt{\tau_w/\rho}} \tag{40}$$

5.1.2 Conditions

Maximum test conditions in the Aeroacoustic wind tunnel, allow for a flow velocity up to $216km/h$, with Reynolds number limited to 324000 based on a $0.1\sqrt{S}$. The proposed boundary conditions for the numerical simulations are limited to this to keep any hope of eventual validation. Since the effective pressure gradient on the flat plate is caused by the lift of the nearby airfoil, its magnitude strongly depends on the dynamic pressure upstream of this airfoil. The maximum flow velocity is therefore desirable and is set as the inflow condition to the domain. However, it was eventually concluded that speeds above $40m/s$, would likely introduce too much sound originating from other components and would exceed the acceptable aerodynamic load for a proper hot-wire set-up.

The two NACA 0018 airfoils with a chord length of $c = 0.2m$ are added such that the centre of flat plate chord line and airfoil chord lines are always placed along a y-axis. Following this definition, the only degrees of freedom left are the height of the airfoils with respect to the flat plate and a rotation along the middle point of its centre line. This makes the set-up referred to as the "default" configuration to be the centre of the pressure gradient generating airfoils chord line to be at $\{0.5 \quad \pm 0.1 \quad 0\}$, parallel with the chord line of the flat plate.

Table 3: Mesh configuration number

Height \ AoA	16°	10°	8°	6°	5°	4°	2°	0°	−2°	−4°	−5°	−6°	−8°	−10°	−16°
default $+30mm$														9	
default $(y = 0.1m)$	25	24	23	22	21	20	19	1	2	3	4	5	6	7	8
default $-10mm$												14		10	
default $-15mm$												15		11	
default $-20mm$												16		12	
default $-25mm$												17		13	
default $-30mm$												18			

5.2 Zero pressure gradient results

Since even in configuration 1 of table 3, s pressure gradient is generated, an additional simulation and measurement is performed for a flat plate without airfoils close to it. In theory, this should indeed result in a zero pressure gradient. Still, the inevitable non-zero thickness of a real-world case warrants the presence of some acceleration and deceleration and thus effectively, in some sort of pressure gradient. This should be permissible as long as the gradient is relatively small along the flat section of the plate and thus the boundary layer is uninfluenced for most of its length. In figure 8 these results are presented with the additional results from Drela's XFoil. This panel method provides fast results by applying a potential flow panel method, which is especially applicable to the situation without external airfoils. Besides the conditions formulated in section 5.1.2, a forced trip location is defined at $x/c = 0.1$ for both the top and bottom location of the flat plate and in coherence with the trip strip location of the experimental set-up.

As could be expected, different behaviour is spotted in the domain $0 \leq x/c \leq 0.1$, as the experiments show real-world behaviour of the laminar boundary layer up till the trip strip, the XFoil results assume a very sudden transition from laminar to turbulent in a discrete fashion and the RANS results do not show laminar behaviour at all. This is not problematic since the main area of focus lies after this domain. The rest of the trend behaviour aligns relatively well, except for the experimental data showing a relatively larger pressure coefficient. Additionally, when looking at the first pressure location, a small deviation between the two sides of the experimental data can be spotted, indicative of a stagnation point not perfectly located at the tip of the flat plate.

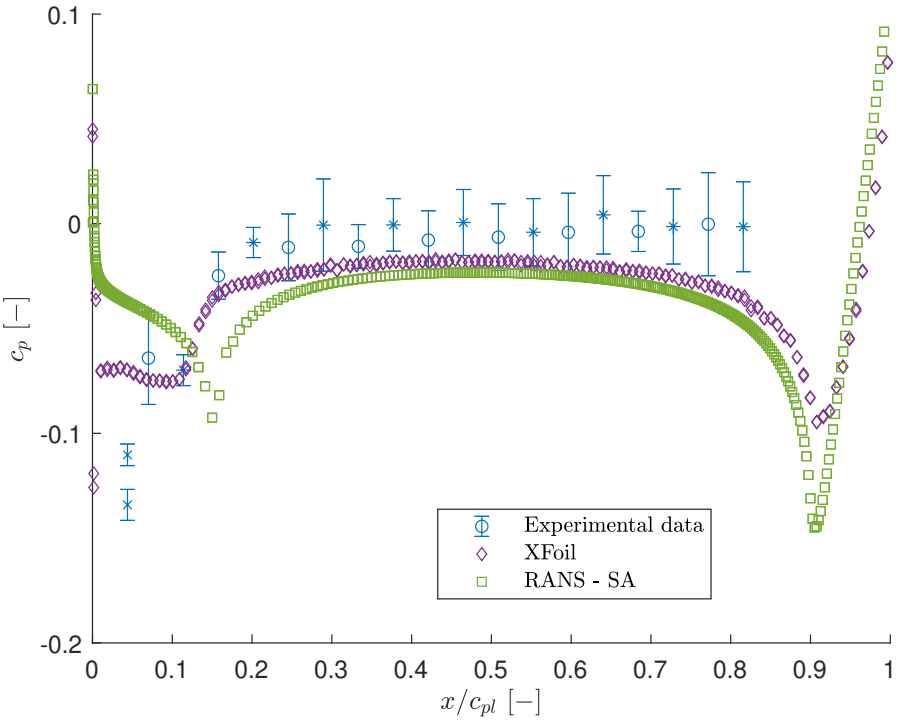

Figure 8: The pressure distribution on the flat plate without airfoils. In the experimental data x indicates leading-edge nodes, o indicates side one nodes, $*$ indicates side two nodes and the bin gives the standard deviation.

5.3 Non-zero pressure gradient results

The configurations of table 3 result in field solutions, to which in the visualization tool Paraview [2], the gradient of the pressure is added. This makes the number of output fields to be twenty-one for every node in the solution field and on its boundaries. It does, however, not provide the boundary layer properties that are desired directly, as this is not a directly modelled property of the governing equations. In order to extract these properties from the solution field, equations from section 3 are applied in a set of scripts further explained in appendix A. One of the parameters most of interest is the β pressure gradient parameter plotted in figure 9.

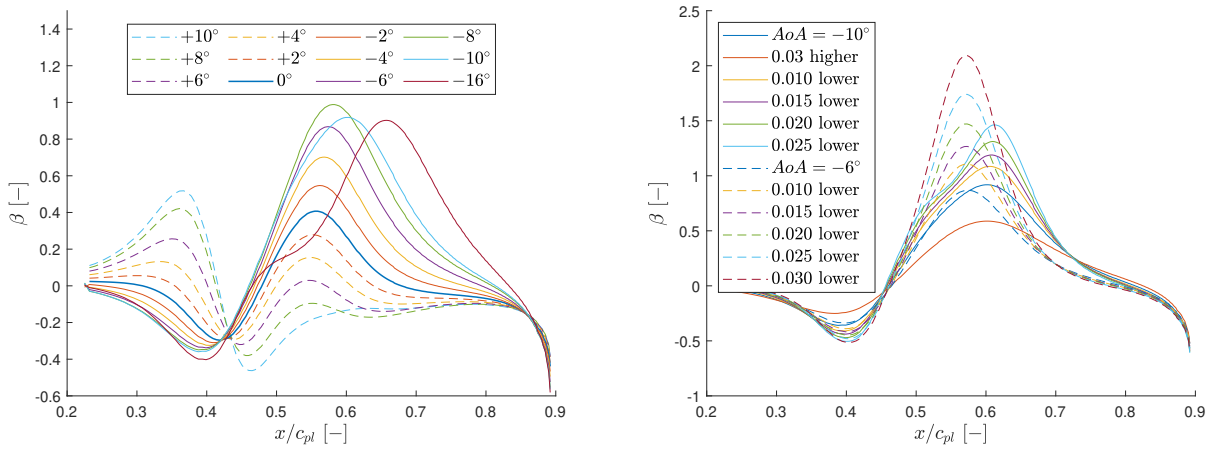

(a) Influence of the angle of attack

(b) Influence of the airfoil normal distance

Figure 9: β pressure gradient parameter, for the configurations presented in table 3 and default height $y = 0.1m$

In the graphs of figure 9 four main trends can be observed. Firstly looking at figure 9a, it is shown that with an increase in AoA, the maximum β-value found increases and slightly moves aft along the flat plate shifting the projected peak. This is not the case where the airfoil is moved up and down as shown in figure 9b, as the peak β-value is still significantly influenced by the height but its location is more static. Making height adjustments more advantageous in precise control over the desired measurement location compared to an AoA adjustment.

Secondly, the width of the β-peak is significantly influenced by the AoA but again not by the height. This is remarkable, as the span in the x-direction appears to have an inverse trend with the length of the projected gradient along the x-direction as visible in figure 9a.

Thirdly, while the maximum β value is significantly influenced by both the AoA and airfoil height, the minimum value seems to be relatively unaffected, all centred around the symmetric case of $AoA = 0°$ where the extremes are located at an equal distance from a point just slightly ahead of the airfoils geometric centre and both with an amplitude of 0.5.

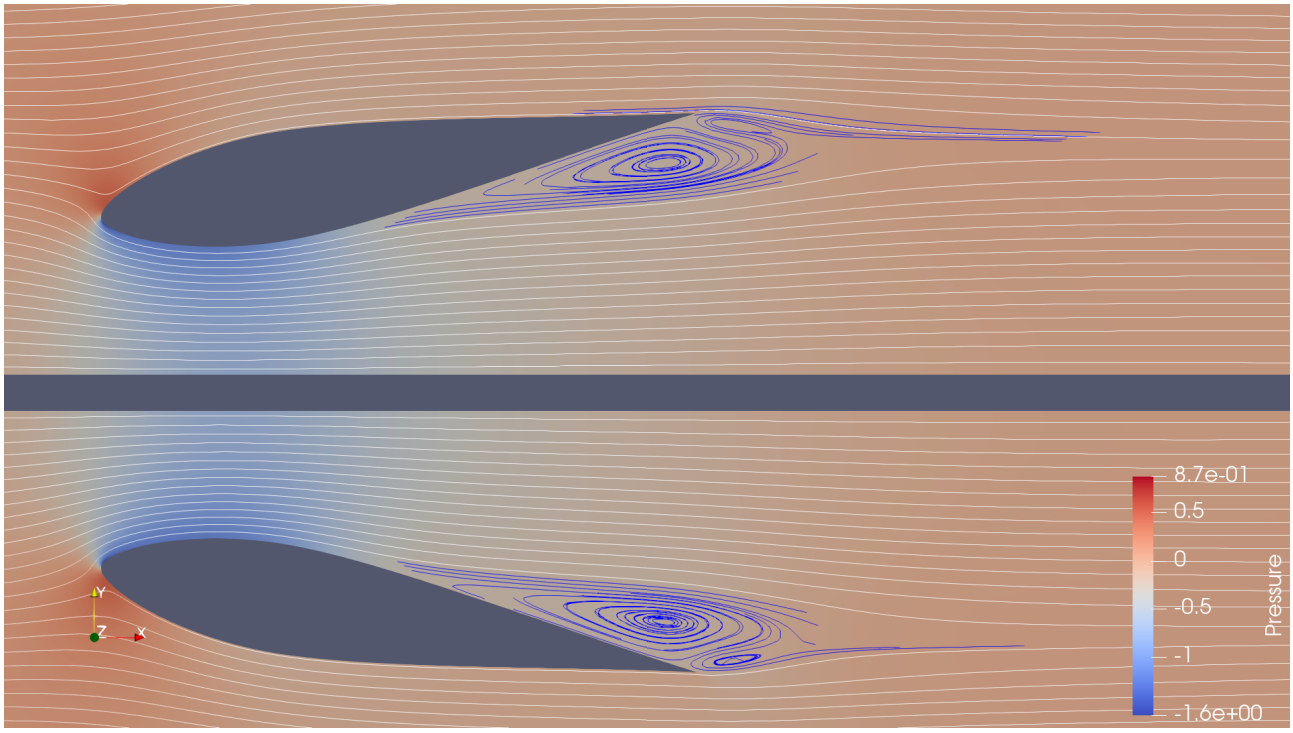

Figure 10: Pathlines in the pressure field of configuration 13 (see table 3), where the white pathlines are seeded $5cm$ in front of the leading edge and the blue pathlines are seeded in separation region.

Finally, in the case of separation behaviour as shown in figure 10 and the solid light blue profile in figure 9a, the projected gradient diminishes and the resulting effective gradient is mostly produced by separation bubbles created in the wake of the airfoil. These bubbles are indicated by the blue pathlines of figure 10 and are located significantly more aft, consequently also shifting the beta peaks in figure 9 aft.

A most important notion about the separation behaviour to be made is that it seriously influences the trustworthiness of the results, as they could indicate some form of transient behaviour that is not captured in steady state. In addition, it might also result in new mechanisms for the generation of noise, potentially skewing any measurement of the trailing edge noise measurements. Measurements exceeding an angle of attack of six degrees are therefore strongly dissuaded.

5.3.1 Trailing edge boundary layer properties

Although the goal of the set-up is to mimic the flat plate behaviour, some influence of the trailing edge geometry can not be excluded. As such, not only the boundary layer properties on the flat section are of interest but also the properties at the trailing edge discontinuity. In figure 11 the integral boundary layer properties along the x-axis are plotted against the angle of attack and normal distance variation.

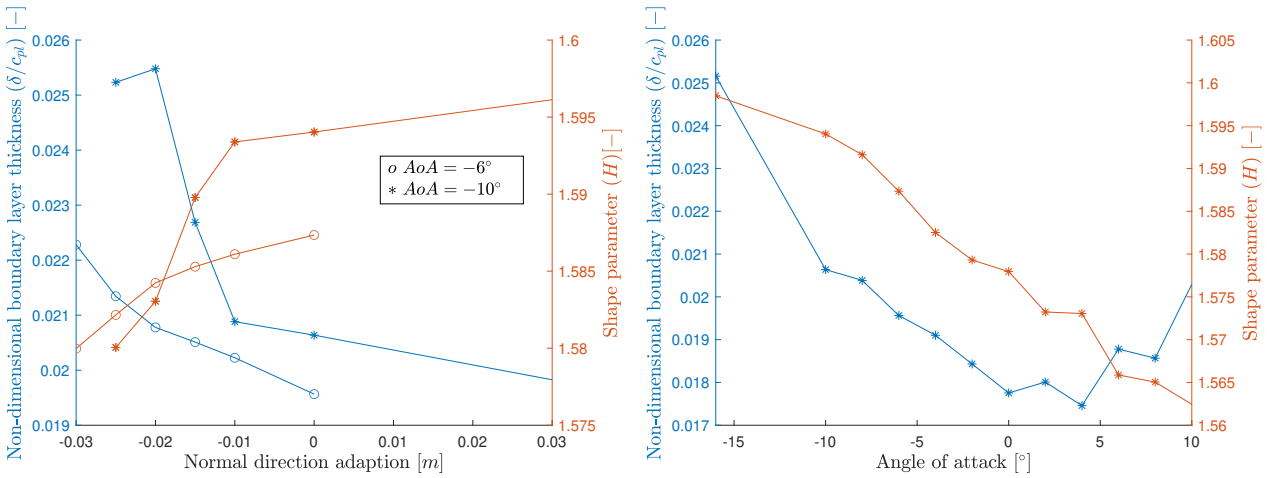

(a) Influence of the airfoil normal distance with respect to the default value $y = 0.1m$.

(b) Influence of the angle of attack at the default height $y = 0.1m$.

Figure 11: Boundary layer integral properties (δ and H) at the trailing edge.

5.3.2 Grid convergence

In reviewing the solution quality an often-used technique is a so-called grid convergence study. In this study, a finer version of the original grid is used to study the effect of the discretization error. This discretization error is a result of flow structures smaller than the cell size that might be averaged out by being smaller. That these structures are averaged out is in principle not objectionable as long as their effects are not dominant on the effect under investigation. In this case, this would be the non-dimensionalized pressure gradient (β). The only relatively unconstrained discretization occurs in the unstructured domain. In addition, this is also where the largest cells are located as visible in figure 12a. This domain is, therefore, a good location to start the grid refinement study in. Two refinement grids where created where the number of nodes was doubled on the domain edges connected to the unstructured domain. This resulted in an increase from $N = 111429$ nodes to $N = 114244$ (figure 12b) and $N = 142073$ (figure 12c). While that may give the impression of only a small refinement, it should be taken into account that the vast majority of cells are located in the more restricted structured domain. The refinements resulted in a non-dimensionalized pressure gradient distribution as presented in figure 12d, where it can be seen that no large difference occurs between the default discretization represented by the blue line and the refined grids represented by the markers. In quantifying this performance a bit more thoroughly, the absolute difference between the default values and those produced in the refined grids was plotted in figure 12e. In this figure, it can be seen that the deviation from the default is less than 0.1% at the locations of major interest (near the gradient peaks) and that the maximum values are created as the gradient approaches the zero line with a less reliable gradient extraction. Based on these results it can be concluded that the discretization falls within engineering accuracy.

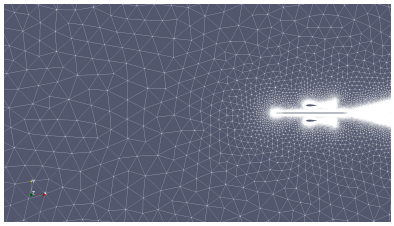

(a) Default discretization.

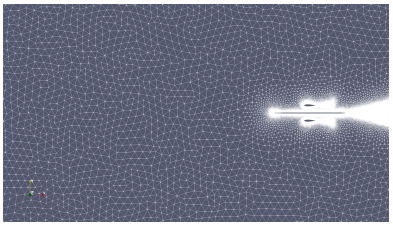

(b) First refinement.

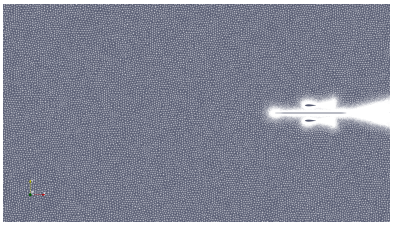

(c) Second refinement.

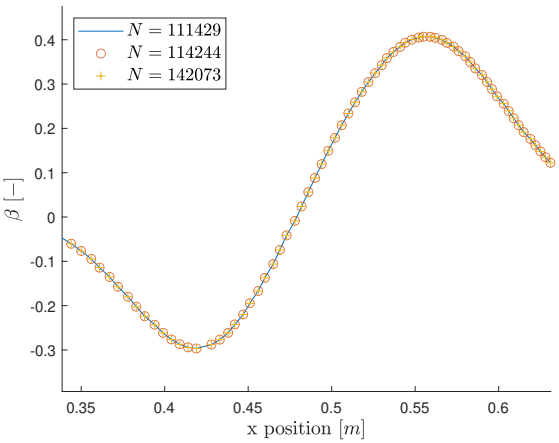

(d) Non-dimensionalized pressure gradient (β).

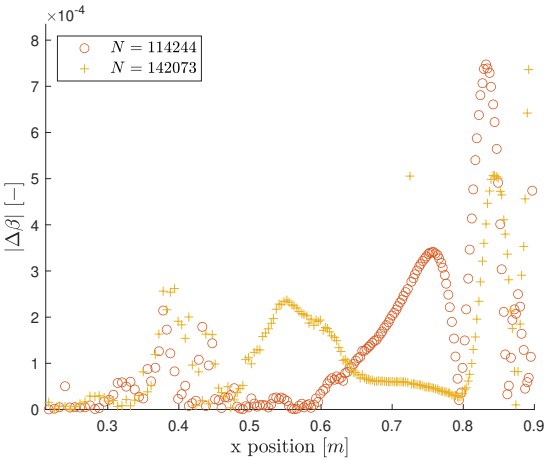

(e) Absolute difference in β.

Figure 12: Grid refinement in the unstructured cells

5.3.3 Solver convergence

Next to the discretization error, another source of inaccuracy with respect to the real world is the solver's convergence, or more accurately, the lack of convergence. This is related to the residuals mentioned before. The most simple way to visualize this is by regarding the mass balance equation. If the mass residual is non-zero, then mass is either created or destroyed. As such, an allowable error is set as exit flag for a typical iterative scheme where the solver will keep iterating until the permissible error is reached or the maximum number of iterations is reached. Reaching this permissible error is referred to as a converged solution and for the simulations performed this was reached by setting the `RMS_VELOCITY-X` limit to 10^{-14}, which showed across configurations to be the slowest converging residual. Typically the pressure equation would show a residual around $10^{-15.5}$, the vertical velocity component residual $10^{-14.75}$ and the turbulence term (ν) residual to be 10^{-17} upon convergence. This means that the error present due to terminating the iterative process at this point is far within the minimal value that can be validated in the proposed measurements.

5.3.4 Quasi-one-dimensional pressure calculation

Common sense and simplified analysis are often a great way to interpret the results of complex calculations such as the ones performed in most CFD packages. Looking at the flow field for an angle of attack of minus four degrees as shown in figure 13. As might be expected, as the y-component of the velocity vector becomes zero, the path-lines become horizontal. At these locations, only the y component of the velocity vector contributes to the total pressure, as it is the only non-zero vector component. This means that the total pressure at these locations can be expressed in equation 41

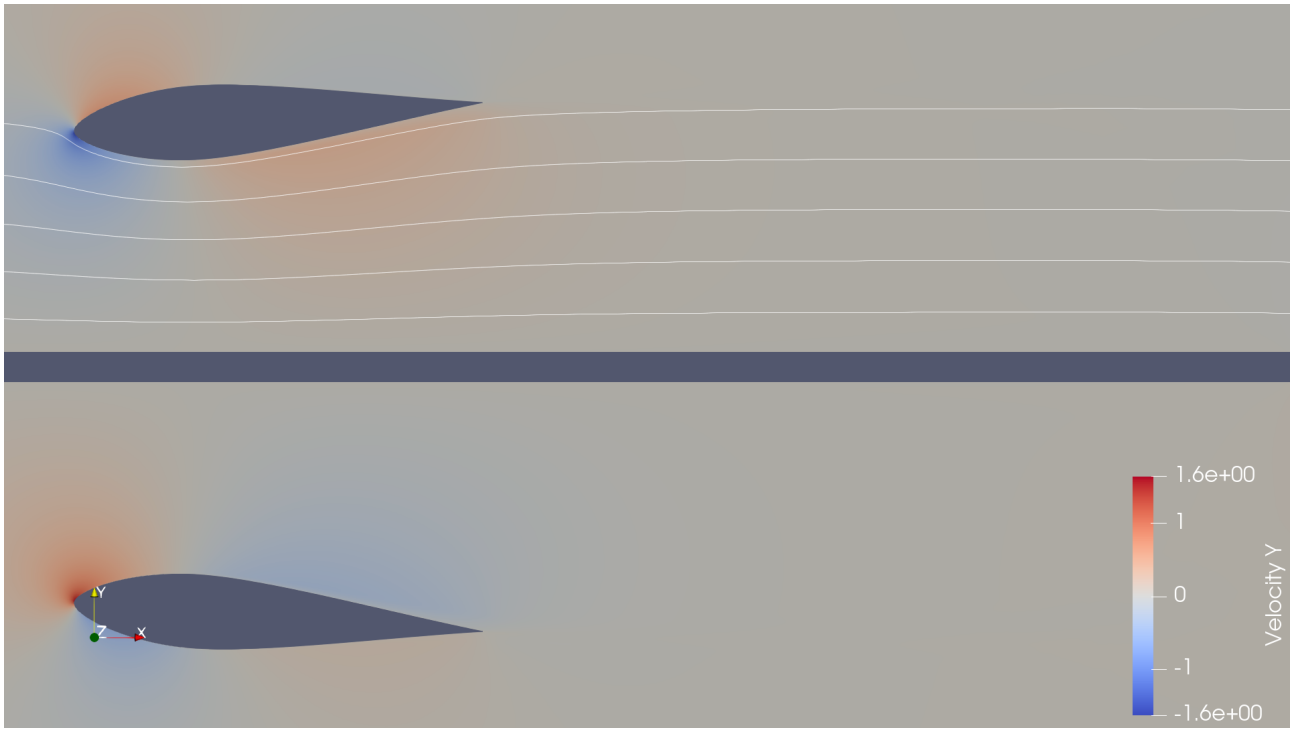

Figure 13: Pathlines plotted in the non-dimensional y-velocity component field for $\alpha = -4°$.

Assuming an inviscid and incompressible (the CFD result is already incompressible) one-dimensional case, the mass flow rate through a virtual surface normal to the flow direction and located at the throat can be described using equation 42. As the streamlines become horizontal after the trailing edge and since there will be no flow normal to these streamlines, a similar surface behind the airfoil should result in the same mass flow rate. This allows for the expression in equation 43 to be created. As the properties behind the airfoil return to the far-field condition, we indicate the properties at this second virtual surface by the subscript $[...]_\infty$, while the subscript $[...]_k$ is used in the virtual surface in the throat. This means that the height of the virtual surface in the throat is indicated by h_k, while the height of the surface behind the airfoil is indicated by h_∞, without it necessarily being a far-field property. The width of the surfaces is indicated by w which is in the z-direction of figure 13, while v in this case indicates only the x-component of the velocity vector.

$$P_t = P_s + \frac{1}{2}\rho v_x^2 \tag{41}$$

$$\frac{\partial m}{\partial t} = \rho w h_k v_k = \rho w h_\infty v_\infty \tag{42}$$

$$v_k = \frac{h_\infty}{h_k} v_\infty \tag{43}$$

As the total pressure should not change along the streamlines and thus should be the same through both virtual surfaces an expression can be made for the difference in static pressure as presented in equation 44 by manipulating equation 41. Dividing out the dynamic reference pressure then results in the difference of pressure coefficients as given in equation 45, while only requiring the two virtual surface heights. For the configuration in figure 13 in the wind tunnel experiments of section 6 these heights were measured to be $h_k = 73mm$ and $h_\infty = 96mm$

$$P_\infty - P_k = \frac{1}{2}\rho v_\infty^2 - \frac{1}{2}\rho v_k^2 = \frac{1}{2}\rho v_\infty^2 \left(1 - \left(\frac{h_\infty}{h_k}\right)^2\right) \tag{44}$$

$$\Delta C_p = 1 - \left(\frac{h_\infty}{h_k}\right)^2 = 1 - \left(\frac{96}{73}\right)^2 \approx -0.73 \tag{45}$$

When reviewing the pressure coefficient distribution on the flat plate in this CFD configuration, as given in figure 14, the amplitude matches the prediction of equation 45 very well. Additionally, the location of this peak seems to be located near the measured throat. This provides confidence in the CFD results.

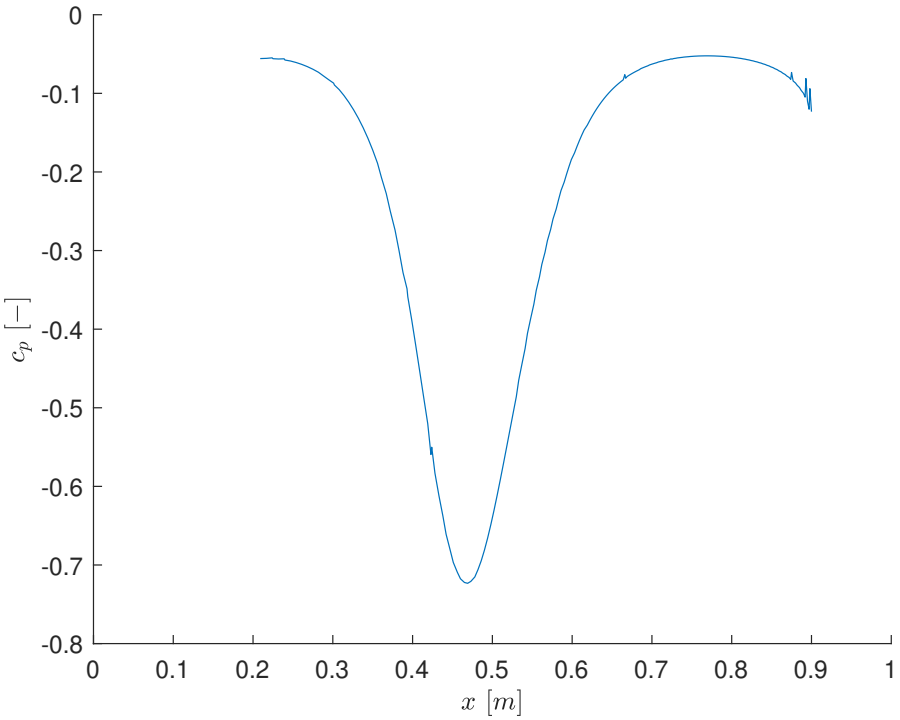

Figure 14: Static pressure coefficient on the flat plate of figure 13.

6 Experimental Setup

Numerical simulations give a relatively inexpensive and full-field solution of the desired problem but make many sacrifices concerning modelling accuracy, numerical errors and an inability to validate solutions. A prime example is the closer problem discussed in section 4.2, where the absence of an analytical solution is solved by averaging and thus capturing the complex effects in a single variable. It is for these kinds of inaccuracies that empirical validation is needed for any case that can not be generalized to a sufficient extent.

6.1 The Aeroacoustic Wind Tunnel at the University of Twente

The wind tunnel at the Faculty of Engineering Technology of the University of Twente originates from the 1970's but was converted to an aeroacoustic wind tunnel in 2001. In 2018 it was further improved to reduce the cut-off frequency. In the current configuration a velocity of $60m/s$ can be achieved with a $132kW$ motor while maintaining a maximum turbulence intensity of 0.08% [36].

6.2 Wind Tunnel design adaptations

Many experiments have been performed in the open test section in the past and in order to accommodate some variety in configurations, a framework referred to as the Open Test Section (OTS) has been installed in the past. Contrary to the name, this section is not a fully open part of the wind tunnel, but rather a semi-open section, bounded by the top and bottom as shown in figure 15a. The bottom and top sections both contain a large bearing allowing for a change in the angle of attack of the entire test set-up, while the open sides allow for the measurement of acoustic effects without as many reflections as would occur in the closed section of the wind tunnel.

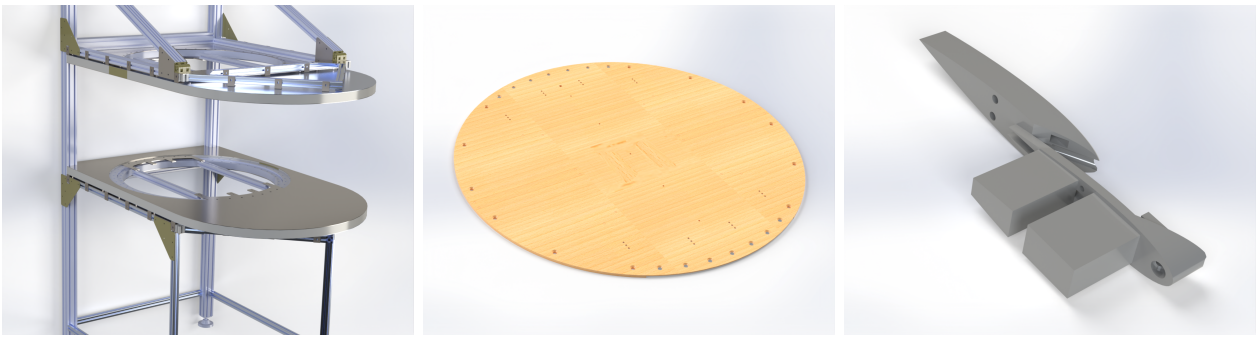

(a) Section of the OTS to be used. (b) Renewed disk. (c) Renewed probe support holder.

Figure 15: Mounting structures of the experimental set-up.

This OTS also allows access to measurement devices in variable locations and in an effort to automate these measurements, a three-axis traversing system is part of the standard equipment, further described in section 6.5. On this traverse system, an airfoil will be mounted preventing interference of the traversing system with the free-stream, while maintaining a large measurement domain.

On the other opening of the OTS, the Bionic M-112 Acoustic beamformer camera by CAE-systems is used to measure the noise using the principles described in section 6.6. It has a sampling frequency $48kHz$ using a $1m$ sampling array consisting of 112 microphones each with a frequency range of $10Hz$ till $24kHz$.

6.2.1 Open Test Section design adaptation

In order to secure the pressure gradient generating airfoils at mentioned positions, a small redesign is needed. However, in the current design of the OTS, the mounting of the pressure gradient generating airfoils, mentioned in section 5.1.2, unfortunately, interferes with some of the mounting structures. This results in the need for a total redesign of the rotating disk. For this redesign, the original mounting

points will be reused. Next to this first constraint, the location of the pressure gradient generating airfoil and the maximum machinable element size are also major restrictions. The former was already prescribed in section 5.1.2, but the latter follows from the machines available to the faculty. This has resulted in the renewed design shown in figure 15b, which will be capable of securing all elements properly.

6.2.2 Hot-wire probe holder attachment

To utilize the Dantec Dynamics 55H21 probe support on the traversing system, while excluding the traversing system itself from the flow domain, the probe support is mounted on a wing attached to the traversing system. The most critical part in this setup is the mechanism used to connect the probe support to the wing profile, as this is close to the probe itself and is a potential source of unwanted flow behaviour. For this reason a new probe support holder was designed as shown in figure 15c.

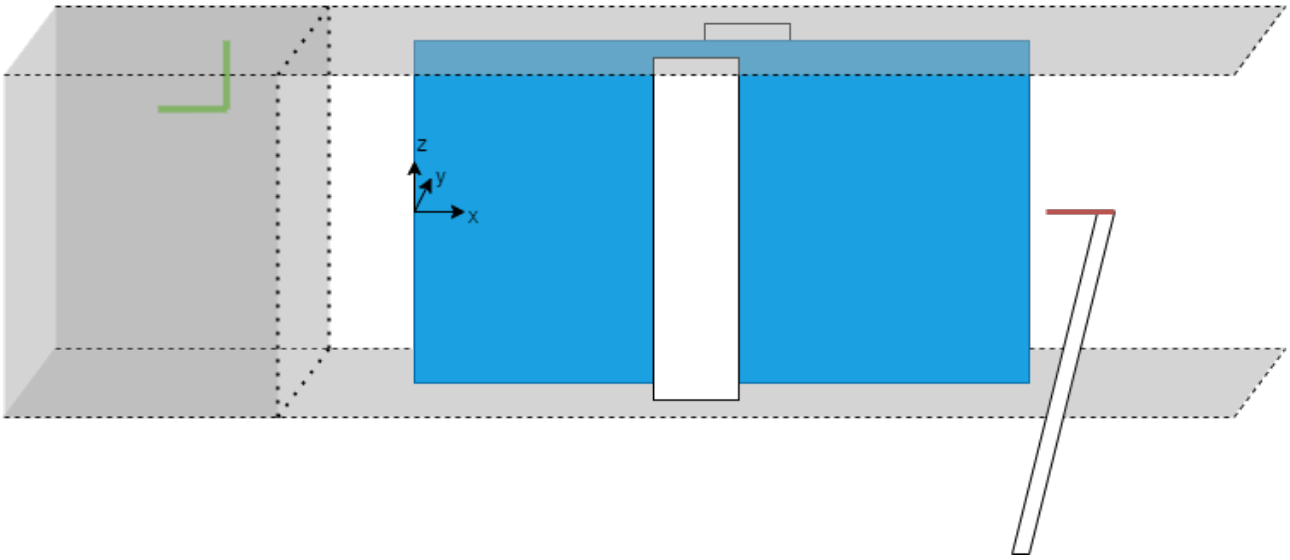

Figure 16: Full measurement setup, where the green probe indicates the pitot tube in the closed section, the blue plate indicates the flat-plate containing the pressure ports and the orange probe indicating the hot-wire probe.

6.3 The Flat Plate Model

The flat plate set-up used is already in the inventory of the faculty of Engineering Technology and its specifications are therefore prescribed. The current pressure ports available on the flat plate are distributed along two lines, diverging from the centre line that is parallel to the mean velocity [15]. The normalized positions of these points are expressed in table 4 and utilized in earlier research in the same wind tunnel by dos Santos[15].

Table 4: Pressure port location.

Side 1

x/c	0.01	0.03	0.05	0.08	0.18	0.28	0.38	0.48	0.58	0.68	0.78	0.88

Side 2

x/c	0.01	0.03	0.05	0.13	0.23	0.33	0.43	0.53	0.63	0.73	0.83	0.93

6.3.1 Static pressure instrumentation

The static pressure is measured with a combination of the Pressure Systems Netscanner Model 9116 and 9216 network pressure boxes used in a closed network. In this network no central distribution of IP addresses is provided and thus the IP addresses used by the boxes themselves act more similar to a MAC address. Using the software `LabVIEW` a TCP protocol is started towards each box, followed by a pressure zeroing and then a loop collecting the pressure data. The script is finalised by closing the TCP connection and writing the gathered data to a `.txt` file. With a sampling frequency of $40Hz$ the pressure is sampled for $20s$ before it is averaged in post-processing using `MatLab`.

6.3.2 Imposing a local pressure gradient

As mentioned before in section 5.1.2, the pressure gradient enacted on the boundary layer of the flat plate will be created by two external airfoils. These airfoils are extruded out of aluminium and mounted to the open test section at $x/c = 0.5$, so that their point of rotation matches the location of mounting. This allows for moving to a different configuration without further disassembling.

$$Re = \frac{\rho u_\infty c}{\mu} = \frac{1.225 * 40 * 0.165}{1.825 * 10^{-5}} = 4.43 * 10^5 \tag{46}$$

At the free stream velocity of $u_\infty = 40m/s$ a quick calculation of the Reynolds number (in equation 46) shows that at these conditions, the instability of the transition behaviour will likely just fit within the length of the airfoil, as these instabilities are reported to occur at $Re \approx 5 * 10^5$ [25]. These instabilities most likely manifest in the form of Tollmien-Schlichtling (TS) waves that are observable due to their distinctive whistle-like sound. This sound is so dominant that it hinders the observability of the flat plate trailing edge noise. To resolve this issue, tripping strips will also be applied to the airfoils at 10% chord length thereby mitigating the generation of TS waves.

6.4 Hot-wire anemometry

The steps in determining the velocity profile integral parameters with the hot-wire anemometry set-up can be divided in two steps. First the data acquisition by the Dantec hardware and consequent transfer to a velocity. Secondly, the post-processing of the discrete velocity profile data and calculation of integral parameters as described in section 3.

The system referred to in the first step of the last paragraph is the Dantec Streamline Pro (its working principle can be found in appendix C). This system automates a lot of the set-up and calibration process in a streamlined GUI. Although, it offers this degree of automation for third-party hot wire probes as well as its in-house manufactured probes and probe supports, the probe selected is the type 55P11 in combination with the 55H21 probe support, all by Dantec.

6.4.1 Velocity profile post processing

Partly due to the disturbance of the free stream by the pressure gradient generating airfoils, the uniformity typically associated by the free stream is greatly reduced. As a result, a point outside the boundary layer can no longer be assumed to be at the conditions defined as the free stream condition. Therefore the largest velocity in the measurement array can no longer be assumed to be u_∞ and thus determining $u_{\delta 99}$ becomes far less straightforward. Another disadvantage of δ_{99} is that it disregards an overshoot of the velocity profile. As shown in section 3.2.1 the velocity profile can be significantly influenced by a pressure gradient acting on it. As the widely accepted boundary layer edge is the point where the velocity reaches an asymptotic value ($u_e(x)$). Weyburne shows that especially for adverse pressure gradients, this location might differ from the location on which 99% of the free stream velocity is reached.

In the example Weyburne gives, an overshoot of the velocity causes a higher peak than the eventual free stream velocity and therefore a stark under-prediction of the boundary layer thickness. In this peak, the first derivative of the velocity with respect to the height is also zero, further giving the false expression that the free stream velocity might be reached [43]. Weyburne argues that one should regard the second derivative as this would be the only indication of real unchanging behaviour.

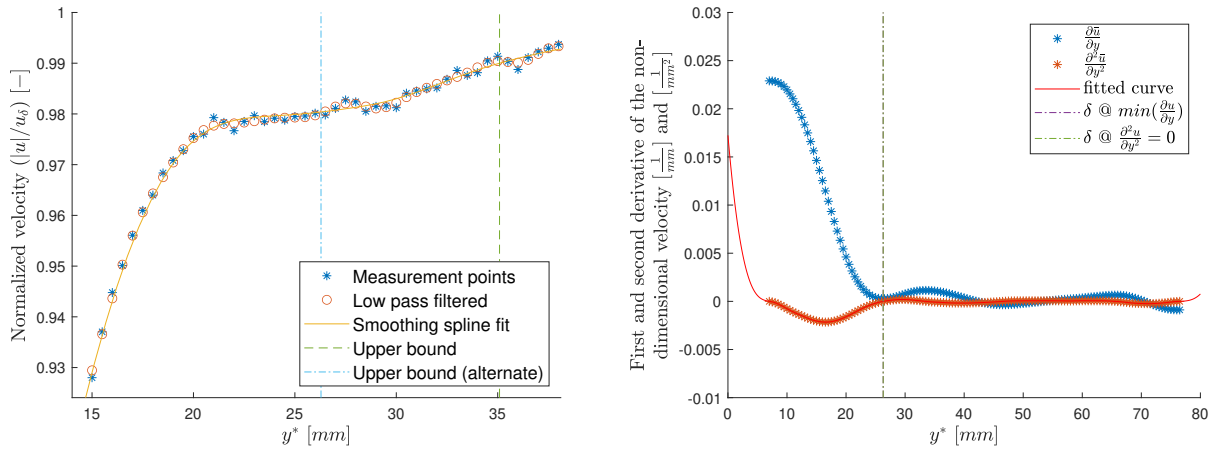

(a) Original measurement points, filtered points and a smoothing spline interpolation against the height (y^*).

(b) The first derivative, second derivative, interpolation and estimated boundary layer edges.

Figure 17: Boundary layer velocity profile with respect to height (y^*), its first and second derivative and the boundary layer height predictions based on these profiles.

As the influence of signal noise increases by every level of differentiation, it will be important to exclude the spatial frequency behaviour below the expected behaviour of the boundary layer itself. A low-pass filter was applied to the complete set of velocity points with the exception of the first 15 nodes closest to the flat plate. In this filter, the sampling frequency is set to one over the mean distance between points (which in theory should be constant) resulting in $f_s = 2m^{-1}$ and the pass-band filter frequency is set to $f_l = 0.4m^{-1}$. Then, as a measure of interpolation, a smoothing spline function is applied with a smoothing parameter of 0.1. That function itself also dampens some of the spatial oscillation. This results in the behaviour shown in figure 17a. The first and second derivatives at the positions of the array `x` are then computed numerically using the Matlab function `differentiate(fit_obj,x)`. The output of this function is then presented in figure 17b, which shows a relatively smooth set of profiles.

From figure 17, the boundary layer thickness is computed in three instances. From the profile as presented in figure 17a, the δ_{99} point is found along the interpolation (`vel_fit(y)`) by solving the condition $u(\delta_{99}) = u_{99} = 0.99max(\vec{u})$ in the form of `d99 = fzero(@(y)vel_fit(y)-0.99*max(v))`. In figure 17a, this point is referred to as "Upper bound". Next, the local minimum of the first deriva-

tive is found. For this to be achieved, another interpolation is applied to the discrete first derivative array `dv` in order to create the function handle `dv_fit(y)`. The local minimum is then acquired with the Matlab function `fminbnd(dv_fit,15,50)` with `15` referring to the left bound of the local minimum search at $y^* = 15mm$ and `50` referring to the right bound. From several plots, it was found that the boundary layer height could typically be expected within these bounds. The found boundary layer thickness with this method is referred to as "Upper bound (alternate)" in figure 17a and "$\delta@min(\frac{\partial u}{\partial y})$" in figure 17b. Finally, in the last instance the point is found for which the second derivative equals zero. This is again achieved by using an interpolation on the discrete second derivative terms which is then used in Matlab's `fzero(fun)` function to find the boundary layer thickness. From figure 17b it can be seen that these last two methods result in almost equal values which is as expected as only numerical errors should contribute to any deviation between the two. As these last two methods provide a workable location of the upper boundary layer edge, only a small correction on the lower edge is applied, resulting in an interpolation function that starts at zero. A numerical integration can then be applied in order to calculate the integral parameters and then a shape parameter. Profiles that show an excessive prediction of the lower boundary layer edge can then be marked and where the prediction of the upper limit deviates more than a percent between the two methods aswell. Filtering out these obliviously wrong estimations results in a dataset for comparison with figure 11b.

6.4.2 Turbulence intensity

As the hot-wire measurements provide a transient signal, it will be possible to calculate the turbulence intensity for behaviour captured in the measurement sample. This is mainly limited by the sampling frequency and the sampling time. In the case of lower frequency behaviour than limited by the sampling time (longest time between samples), the behaviour is cancelled out by the averaging in that time sample. Meanwhile, when the frequency behaviour is higher than the Nyquist frequency (half of the sampling frequency) aliasing can occur, which will result in a loss of information of that frequency behaviour. As such the highest frequency behaviour is limited by the sampling rate (shortest time between samples). On the basis of the experience of lab technicians who performed similar experiments a sampling frequency of $f = 10kHz$ with $N = 50k$ samples was used resulting in a sample time of $t = 5s$ which would capture the most relevant turbulence behaviour.

In contrast to the RANS-SA simulations, this then results in a time-dependent array of velocities at each measurement point. Referring to this array as $\vec{U}$, its mean is then $\bar{U}$. These values can be used to calculate a turbulence intensity in equation 47, which is a measure of the flow rate variation with respect to the average flow rate. Meanwhile, the transport quantity of many turbulence models is the kinetic turbulent energy (k), but for most commercial packages this translation occurs within the `GUI` using equation 48. This allows for the comparison of empirical and numerical data using the turbulence intensity. Unfortunately, the Spallart-Allmaras model does not use this transport variable (instead using the Spallart-Allmaras variable) and therefore does not allow for this comparison.

$$I = \frac{rms(\vec{U} - \bar{U})}{\bar{U}} \tag{47}$$

$$k = \frac{3}{2}(\bar{U}I)^2 \tag{48}$$

6.5 Traverse system

Traversing the hot-wire probe along the field of interest is achieved using the Dantec 9041T333. It has a range of $1010mm$ and a resolution of $6.25\mu m$ on all axes. The traversing system is directed by a 9041T019 motor controller whose interface is integrated with the measurement software for the hot wire measurements, all from Dantec. A benefit of this package is the amount of streamlining and guidance the software provides in the measurement process.

6.6 Far-field noise measurements

The far-field noise is the prominent effect to be studied and as such, it will be captured using a microphone array, but many things in even the most controlled set-up will produce noise, so it is important to distinguish noise production locations. As hinted to before, this can be achieved with the beamformer technique often used in other signal applications, such as radars, WiFi and human hearing. A short introduction to this technique can be found in appendix B, but the most important things to know are the distance of the microphone array to the expected noise source and the frequency used. For all measurements, the distance to the microphone array has been set to $L = 2.01m$, the high pass filter to $f_{hp} = 1500Hz$, the low pass to $f_{lp} = 2500Hz$ and the sampling time to $t = 5s$. These settings applied to delay and sum algorithm showed enough fidelity to distinguish the two sources as showed in figure 18.

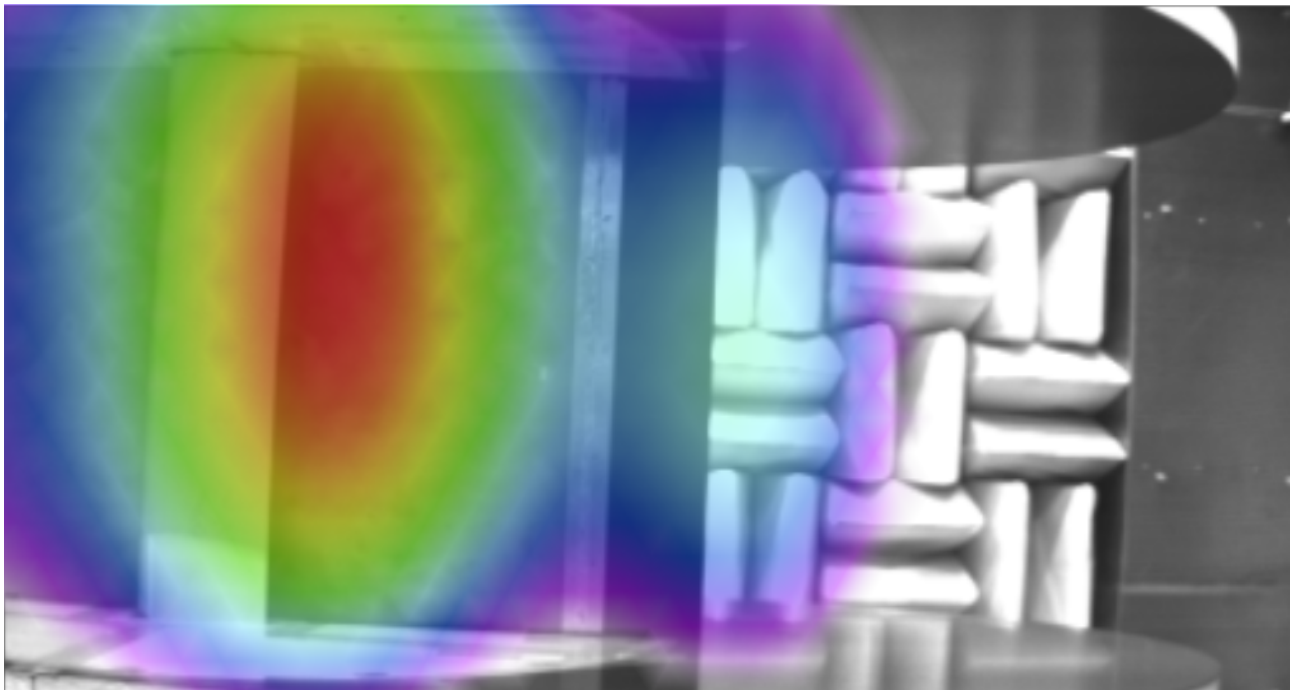

Figure 18: Beamformer output map applied to configuration number 1 of table 5, showcasing the trailing edge noises from both the external airfoils, as well as from the flat plate.

6.7 Test conditions

In the validation of the numerical results, significant efficiency can be obtained by strategically choosing the configurations, since changing the configuration requires a relatively large amount of time. Factors like the complexity of changing parts, connection of new measurement devices, device calibration, and the settling time of the wind tunnel and its cooling system subtract from the available finite time resources. As such, not all configurations from the numerical study will be repeated in the empirical process, but the empirical configurations can be found in table 5. In addition to these configurations, the case without a pressure gradient generating airfoil is also added as a base reference.

Table 5: Experimental set-up configuration number

Height \ AoA	16°	10°	6°	4°	0°	−4°	−6°	−10°	−16°
default $+30mm$							10	11	
default	1	2	3	4	5	6	7	8	9
default $-30mm$							12	13	

7 Experimental Results

7.1 Static pressure measurements

Since the static pressure consists of the influence of the local flow added to an atmospheric component, it is dependent on both the experiment configuration and the atmospheric conditions at the time of measurement. As most pressure sensors including, those used in this experiment measure a pressure difference, this ambient atmospheric component is usually added afterwards. However, since there is no atmospheric effect modelled in the CFD calculations, its contribution does not offer additional insights of interest. Therefore, instead of reviewing the static pressure, the static pressure deviation is studied. This makes the results comparable regardless of time and date of measurement.

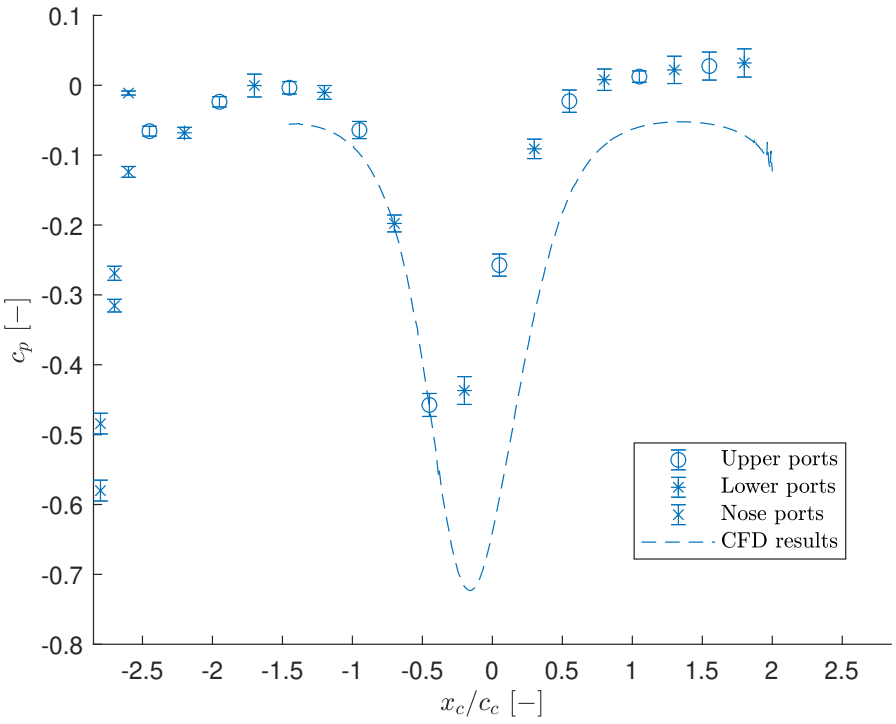

Figure 19: Plot of the coefficient of pressure against the x location along the flat plate normalized by the chord of the airfoil, with $x = 0$ at the airfoil's point of rotation. These pressure gradient-generating airfoils are at $\alpha = -6°$.

As such, figure 19 can be constructed (while the other configurations can be found in appendix D.3 where the global coordinate system is located such that $x = 0$ at the points where the pressure-generating airfoils rotate about. Since the pressure gradient is more influenced by the length of the airfoils than the length of the flat plate, the chord of the airfoil (c_c) is used for the normalization of the x-axis. Meanwhile, the y-axis is normalized using the dynamic pressure, resulting in the coefficient of pressure.

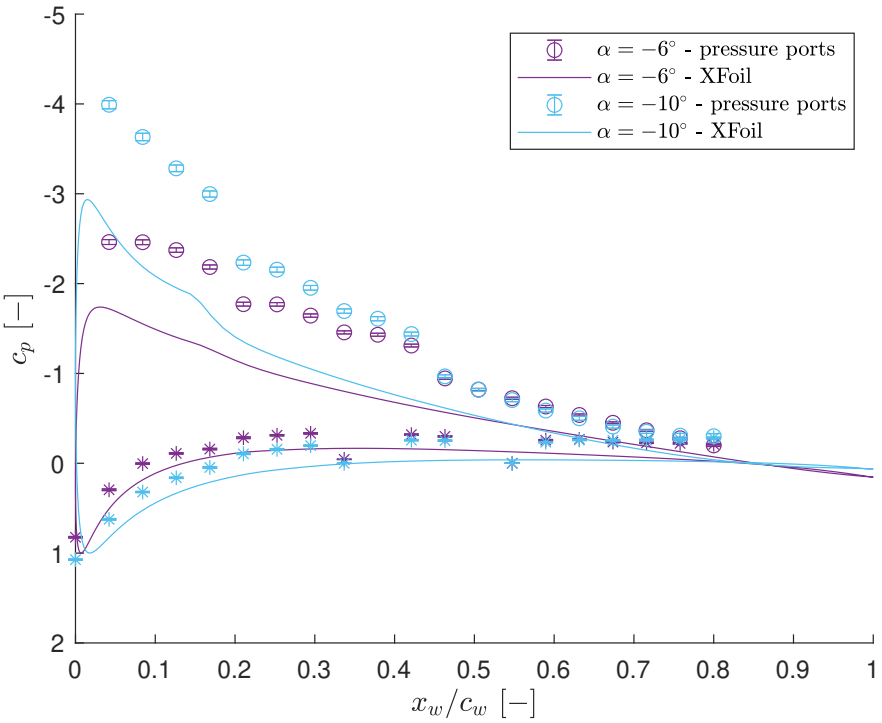

Figure 20: Coefficient of pressure on the pressure gradient generating airfoils for the closest normal distance ($y = \pm 0.07$).

As separation behaviour on the pressure gradient generating airfoils is most definitely possible, aided by the interaction with the flat plate, the static pressure of these airfoils is plotted in figure 20 for the highest predicted pressure gradient values. Presented against the length over the chord of these airfoils (x_w) and normalized with the total chord length (c_w) these measurements allow for comparison against results from a panel method like `XFoil`.

7.2 Boundary-layer measurements

As mentioned before, the boundary layer velocity profile is measured using a hot-wire setup. Since this technique relies on an accurate transfer function for translating the dissipated electrical energy to an absolute velocity, an accurate calibration is most important. Unfortunately, the calibration was found to be tainted due to a defect in the far-field velocity measurement setup. Specifically, the data handling of the pitot tube. This makes the amplitude of the transfer function to be unreliable, but fortunately, this static gain cancels out in the determination of the boundary layer thickness and in the calculation of the boundary layer integral parameters. As such, the post-processing steps in section 6.4.1 could be applied to result in figure 21[3]. When normalized by the boundary layer edge velocity also a comparison of the empirical and CFD profiles is possible of which two results are provided in figure 22 that show the general trend of all profiles.

[3]Unfiltered results can be found in figures 30 and 31 of appendix D.1

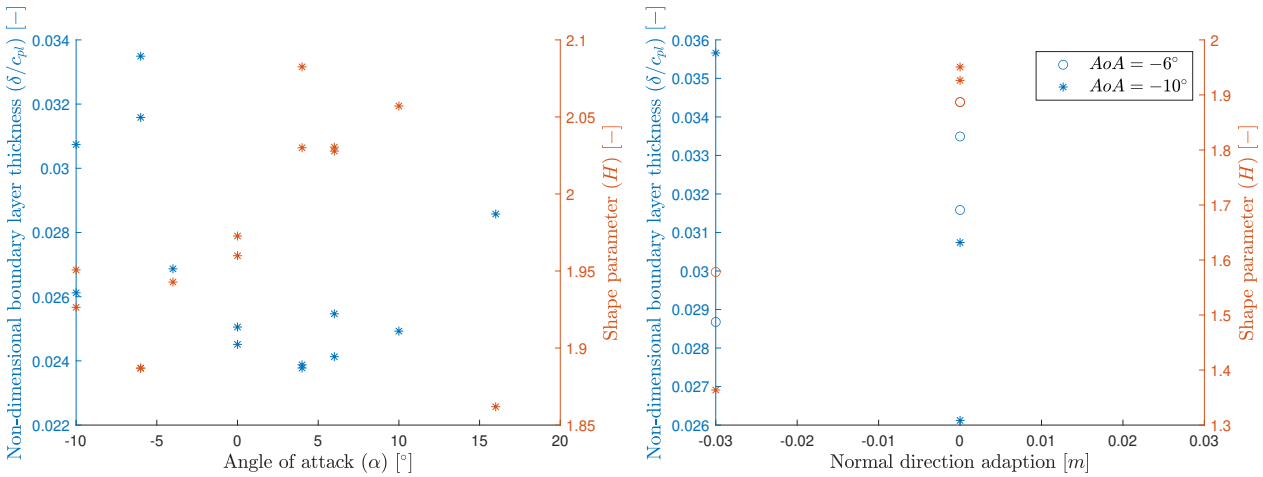

(a) Concerning the angle of attack.

(b) Concerning the normal distance.

Figure 21: Boundary layer integral properties (δ and H) at the trailing edge with respect to the angle of attack at the default height of $y = 0.1m$.

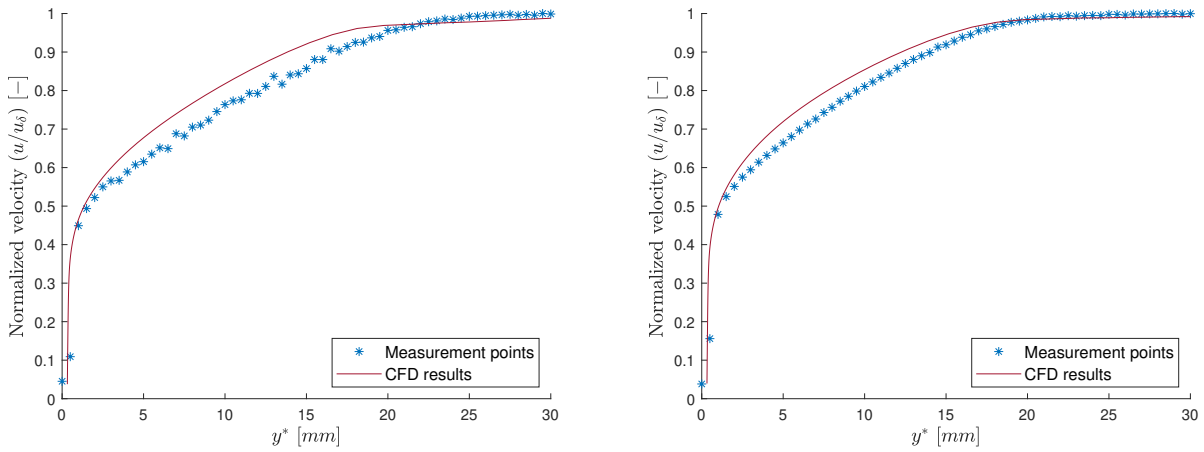

(a) $\alpha = -16°$

(b) $\alpha = -4°$

Figure 22: Boundary layer velocity profiles at the flat plate trailing edge against the normal distance (y^*) for negative angles of attack of the pressure gradient generating airfoils

Although direct comparison against the turbulence in the numerical scheme is not possible for the reasons mentioned in section 6.4.2, it is still possible to extract the turbulence intensity from the trailing edge measurements and compare them to literature for a case without pressure gradients. As such figure 23a plots the turbulence intensity for the most important configurations with respect to the normal distance to the wall on a logarithmic scale. Unfortunately, the shear coefficient in this location was not measured and thus non-dimensionalizing it to y^* was not deemed beneficial. Meanwhile, compatible profiles were found in the form of figure 23a by Kearney et al.

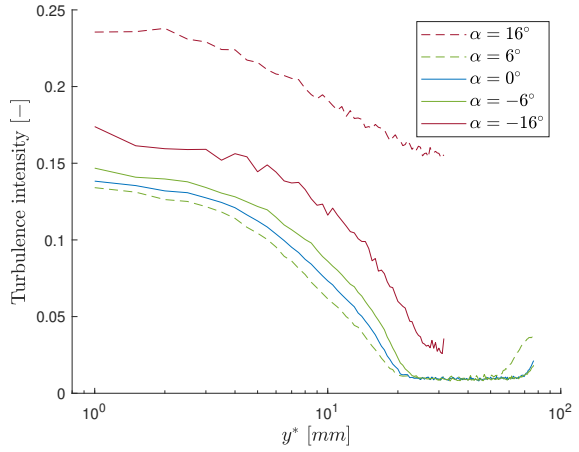

(a) Measured at the flat plate trailing edge for various angles of attack of the pressure gradient generating airfoils.

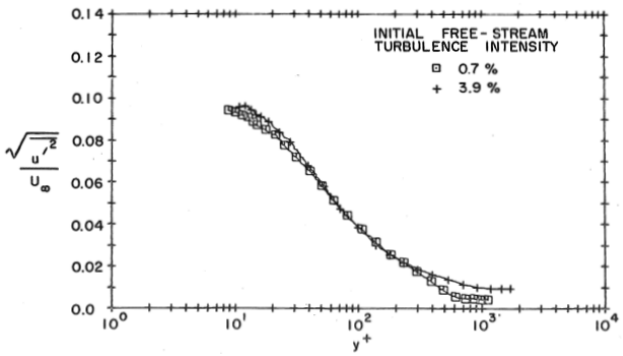

(b) Experimental turbulence intensity profiles near the end of the accelerated region. $Re_H \approx 1430$ [27]. Representing the general trends of turbulence in the boundary layer.

Figure 23: Turbulence intensity in the boundary layer

7.3 Far-field noise measurements

Two examples of the beamformer output maps can be found in figure 24, which show general trends also found for the rest of the datasets (included in appendix D.4). Using the delay and sum beamformer algorithm included in the Noise Inspector software package within the frequency bin $1500Hz < f < 2500Hz$, most results show the behaviour best represented by figure 24a, where the trailing edge noise source of the flat plate can clearly be distinguished. However, in the more extreme cases where separation behaviour likely occurs, such as in figure 24b at an angle of attack of $\alpha = -16°$, the source becomes less distinct although still identifiable[4].

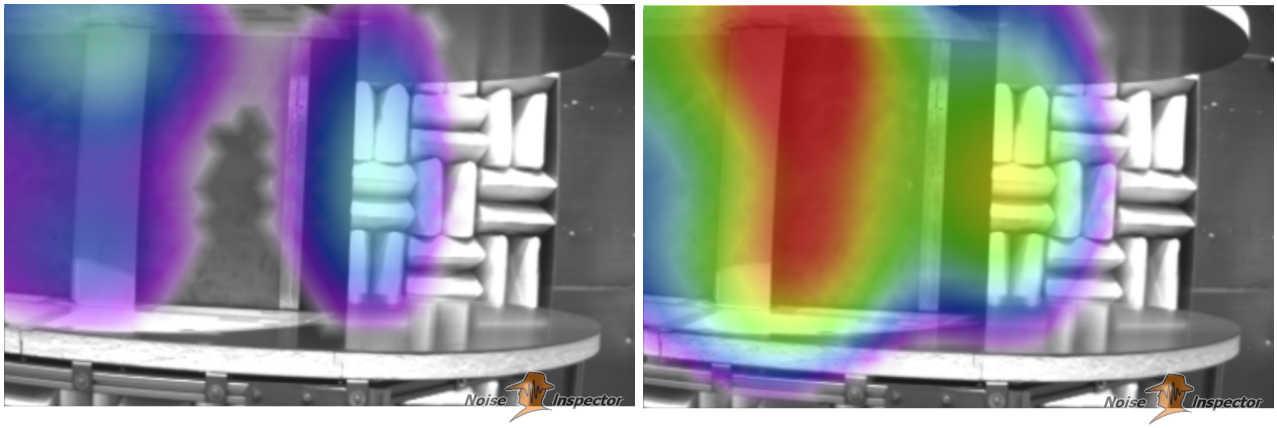

(a) Table 5 configuration 3 (default height ($y = \pm 0.1m$) and $\alpha = 6°$).

(b) Table 5 configuration 9 (default height ($y = \pm 0.1m$) and $\alpha = -16°$).

Figure 24: Representative beamformer output maps regarding the far-field acoustics. The scales of the output maps are from $52.5dB$ (purple) till $58.5dB$ (red) using $p_{ref} = 2 * 10^{-5}Pa$. The frequency bin is $1500Hz < f < 2500Hz$ and the distance from the microphone array to the investigative plane is $L = 2.01m$.

[4] Additional results can be found in appendix D.4

8 Conclusion & Recommendations

As the goal was to alter the turbulence statistics effectively, the question of whether this was achieved can be split into a couple of levels. In none of them, these statistics are directly extracted, but they all relate to at least one term of Amiet's model in section 2.1.

The only term researched not directly found in equation 2, is the pressure gradient. However, as it directly influences the thickness and shape of the boundary layer it is still the premier parameter to indicate the level of equilibrium disturbance to the turbulent boundary layer and thus the turbulence statistics mentioned in equation 1.

8.1 Pressure distribution

From the gradients found in the numerical analysis, a couple of main observations can be made: Firstly, it appears to be that any form of stall behavior on the pressure gradient generating airfoils is detrimental to the effective gradient produced. Secondly, the negative angles of attack seem to create a more significant disturbance to the equilibrium compared to their positive counterparts. However, for the most effective gradient, the distance from flat plate to the wings is of much larger influence than the angle of attack. Thirdly, as an added benefit, this height alteration also influences the location of the gradient peak's to a smaller extent as long as stall behaviour is prevented. From figure 9, it can be seen that significant pressure gradients are achieved, with a maximum gradient of $\max(|\beta|) = 2$. This gradient is representative of a typical airfoil near the centre of the chord length as well, and thus representative gradients can be reached as shown when comparing to table 1. However, more serious gradients such as the one presented in table 2, are still a far reach as this would increase the gradient by a factor of seven, while the current configurations already approach stall limits.

Comparing the pressure static pressure results from CFD to experimental data two main observations can be made. First is the gain difference between the numerical and empirical pressure in figure 19. This might be connected to the difference in pressure on the first location of figure 19, indicating a shift in the stagnation point due to a misalignment of the flat plate. Since it is assumed that most of these discrepancies occur in the mounting set-up, it is advised to CNC machine these parts in order to reduce the possibility of misalignment. Second, the shift in in pressure peak location. This might be caused by the improper built-up of the boundary layer as the wind tunnel starts up with the pressure gradient generating airfoils already at an angle of attack. It is advised to rotate these airfoils to their desired angle of attack when the wind tunnel is in operation in future experiments.

8.2 Trailing edge boundary integral layer parameters

The trailing edge boundary layer integral parameters, as shown in figure 11, show that the shape and thickness of the trailing edge boundary layers can successfully be influenced. Noticeable in this figure are the trends that emerge upon altering the airfoil configuration, especially the difference between height alterations and angle of attack alterations. As a larger absolute angle of attack and a lower height typically result in a more significant pressure gradient, the shape factor seems to decrease at these larger gradients when a height alteration is applied, while showing an increase when caused by negative angles of attack. No explanation was found for this phenomenon and therefore it can be a focus of future research.

The trends found in the numerical data are not reproducible from the empirical data as shown in figure 21. Although in the same order of magnitude, the precision in between measurements seems to be lacking. In figure 21a some form of a bathtub trend is visible, but not at all to the same extent as found in figure 11b. It is hoped that more precise results can be obtained upon a more stable flow temperature and tighter tolerances in construction, resulting in smaller fluctuations between measurements and a more accurate determination of the boundary layer edge.

8.2.1 Turbulence intensity

While not directly an integral parameter, the turbulence intensity along the trailing edge boundary layer is still a product of the same measurements. It can also not be compared against the numerical results but when comparing to the results by Kearney et al. the trends and order of magnitude most definitely concurs. Additionally, also a data trend concerning the angle of attack of the pressure gradient generating airfoils can be found where an increase in the angle results in an increase in the turbulence intensity, excluding the measurement at $\alpha = 16°$, which can be contributed to the separation it will introduce much closed to the measurement location compared to the other configurations.

8.3 Far-field noise

As mentioned in section 7.3, within a frequency band of $1500Hz < f < 2500Hz$, the trailing edge noise of the flat plate is visible in the beamformer map for all configurations. This makes the method of placing pressure gradient-generating airfoils close to the flat plate a suitable option in the research of the trailing edge noise mechanism. Although demonstrating the detectability of the trailing edge noise, it is not yet a true quantification of the noise emitted. This could be achieved by integrating over the frequency bin and area where the trailing edge noise is found to give a more quantifiable answer to the question of how the trailing edge noise is affected by the generated non-equilibriums.

Although working for the configurations mentioned in this report, it is possible that other configurations will result in undetectable trailing edge noise from the flat plate. This is especially the case for a configuration where the airfoils are mounted more aft of the flat plate. In the results presented it is already visible that the dominant sound source is the trailing edge of the airfoils and therefore keeping sufficient distance from the flat plate trailing edge has to be of concern in future research. As the pressure gradients still have to increase near the trailing edge in order to fully simulate typical airfoil behaviour shown in table 2. As such when research approaches such a stage it is likely that pressure-generating airfoils will no longer suffice.

8.4 Numerical simulations

Next to the main research goals, further observations can be made, mainly about the numerical simulations. For the simulations used, a relatively simple turbulence model was used, to reduce the complexity of the simulation. When coupled with the relatively low-order numerical schemes used and simple scenario (without shock or large separation behaviour) much higher performances should be expected and thus a CFL number of around four appears to be incredibly low. The reason for divergent behaviour at higher CFL numbers was unfortunately not found and the sources of these instabilities remain a reason for curiosity.

When the issue mentioned above is addressed, it might also be of interest to experiment with the suitability of using other turbulence models, especially in order to see whether the turbulence kinetic energy parameter can provide insight into the turbulence statistics with a high degree of accuracy and precision. Do these models hold for non-equilibrium conditions with the severity of table 2 and can they substitute the semi-empirical relations currently used in Amiet's approach are the proposed research questions for further research in this field.

Finally, fully studying the turbulent boundary layer trailing edge noise also involves studying the laminar to turbulent transition for realistic cases. In this research, trip strips were applied to force turbulent behaviour after a certain point, but in many real-world cases, such a well-defined location will be unknown. The authors of many turbulence models warn against the use of their models in the prediction of transition behaviour. Furthermore, relaminarization is a potential pitfall for these models and would significantly impact the turbulence statistics. A validated model to accurately model these statistics inside a CFD application without the computational costs of direct numerical schemes or overly large computational models therefore remains highly desirable in the field of aeroacoustics.

Acknowledgments

A few people should be mentioned, without who this research would not have been possible. Firstly, my daily supervisor dr. ir. Sanders. Thank you for the guidance in the field of aeroacoustics, but certainly also in the field of academic writing and even philosophy. As I indicated to prof. Venner at the start of my thesis: "I don't want to do CFD", but for some reason, a lot of fluid mechanics still ends up there (including this work). Dr. Ströer took over my daily supervision for more than half a year and helped me in the form of many hours of discussion about CFD. I think I barely scratched the surface of his knowledge on the topic. Just as important as the people with knowledge have been, so are the people with experience. Thank you Walter and Elise, for showing me and helping me to work with the awesome equipment we have at the UT and for keeping me safe while using it. The things you provide you can not learn from a book. Keeping this list limited only to the people directly involved for the duration of this thesis is not fair to all the teachers who have made a huge impact on me as an academic and as a person. Special mentions go to dr. ir van Garrel, dr. ir. Hagmeijer, prof. dr. ir. Venner, dr. Stoffels and probably a lot of teachers I am forgetting now. Next to these teachers, my fellow students have also been paramount in my academic career until now (special mentions to Nikolaj Even, who has been a great support in writing this thesis). Whether they explained something to me, I learned something from explaining it to them or when they were just part of a community where you can learn so much more than from books, such as the study association W.S.G. Isaac Newton or in the organisation of the Batavierenrace. That only leaves me to thank you, the reader, before I mention the two most important people of this list. Thank you for taking the time to read my work, maybe to even think something of it, or even better, to ask me a question about it. This is especially the case for the graduation committee. Then finally, thank you mom and dad, for many years of complaining, fun moments, sad moments, keeping me motivated during COVID and keeping yourself motivated from the moment I started talking as a kid (it had to be quite early and from my dispuut ODMC, I hear that I often like to do it a lot). Thank you for getting me here.

References

[1] R.K. Amiet. Acoustic radiation from an airfoil in a turbulent stream. *Journal of sound and vibration*, 41(4):407–420, 1975.

[2] Utkarsh Ayachit, Andrew Bauer, Berk Geveci, Patrick O'Leary, Kenneth Moreland, Nathan Fabian, and Jeffrey Mauldin. Paraview catalyst: Enabling in situ data analysis and visualization. In *Proceedings of the First Workshop on In Situ Infrastructures for Enabling Extreme-Scale Analysis and Visualization (ISAV 2015)*, pages 25–29, November 2015. doi: 10.1145/2828612.2828624.

[3] Andre Bakker. Lecture 7 - meshing. In *Lectures on applied computational fluid dynamics*, Courses Computational Fluid Dynamics and Reacting Flows, pages 240–274, Hanover, US, 2006. Darthmouth College.

[4] Axel Blaauwbroek, Hoogen Jeroen van den, Nayim Manik, and Marcel Vliem. *Wind Energy Assignment 4.* As requisite of Arne van Garrel, professor, MSc course *Wind Energy - 201700024*, at the faculty of Engineering Technology of the University of Twente. Enschede, 2021.

[5] P L Bourget. Calibration method for a hot wire anemometer. *Journal of Physics E: Scientific Instruments*, 9(5):353, may 1976. doi: 10.1088/0022-3735/9/5/011.

[6] Joseph Boussinesq. *Théorie analytique de la chaleur mise en harmonie avec la thermodynamique et avec la théorie mécanique de la lumière*, volume 4 of *Cours de physique mathématique de la Faculté des sciences.* Gauthier-Villars, 1903.

[7] Thomas Brooks, Stuart Pope, and Michael Marcolini. Airfoil self-noise and prediction. Technical Report NASA reference publication 1218, National aeronautics and space administration, Hampton Virginia, 1989.

[8] Hans Henrik Bruun. *Hot-Wire Anemometry: Principles and Signal Analysis.* Oxford university press, Oxford, 1995.

[9] Francis H. Clauser. Turbulent boundary layers in adverse pressure gradients. *Journal of the Aeronautical Sciences*, 21(2):91–108, 1954. doi: 10.2514/8.2938.

[10] G. M. Corcos. The structure of the turbulent pressure field in boundary-layer flows. *Journal of Fluid Mechanics*, 18:353–378, January 1964. doi: 10.1017/S002211206400026X.

[11] Armin Cosic, Luc Drummen, Niels Nijland, Ruchira Rupakula, and Marcel Vliem. *Green liquid hydrogen as the energy source for ground equipment on Schiphol airport.* As requisite of Mina Shahi and Banerjee Aayan, professors, MSc course *Energy storage - 201600252*, at the faculty of Engineering Technology of the University of Twente. Enschede, 2022.

[12] N. Curle and Michael James Lighthill. The influence of solid boundaries upon aerodynamic sound. *Proceedings of the Royal Society of London. Series A. Mathematical and Physical Sciences*, 231 (1187):505–514, 1955. doi: 10.1098/rspa.1955.0191. URL `https://royalsocietypublishing.org/doi/abs/10.1098/rspa.1955.0191`.

[13] William Devenport and Stewart Glegg. *Aeroacoustics of Low Mach Number Flows.* Elsevier Inc., 2017. ISBN 978-0-12-809651-2.

[14] William J. Devenport and K. Todd Lowe. Equilibrium and non-equilibrium turbulent boundary layers. *Progress in Aerospace Sciences*, 131:100807, 2022. ISSN 0376-0421. doi: https://doi.org/10.1016/j.paerosci.2022.100807.

[15] Fernanda Leticia dos Santos. Influence of tripping devices in hastening transition in a flat plate submitted to zero and favorable pressure gradients. Master's thesis, University of Twente, Enschede, August 2019.

[16] Mark Drela. XFOIL: An Analysis and Design System for Low Reynolds Number Airfoils. In Thomas J. Mueller, editor, *Low Reynolds Number Aerodynamics*, pages 1–12, Berlin, Heidelberg, 1989. Springer Berlin Heidelberg. ISBN 978-3-642-84010-4. doi: 10.1007/978-3-642-84010-4_1.

[17] Mark Drela. *Flight Vehicle Aerodynamics*. The MIT press, Cambridge, Massachusetts, 2014.

[18] E RG Eckert and Robert M Drake Jr. *Analysis of heat and mass transfer*. Hemisphere Publishing, New York, NY, 1987.

[19] Thomas D. Economon. Simulation and adjoint-based design for variable density incompressible flows with heat transfer. *AIAA Journal*, 58(2):757–769, 2020. doi: 10.2514/1.J058222.

[20] Nikolaj Even and Marcel Vliem. *Assignment 6 - Beamformers*. As requisite of Leandro de Santana, professor, MSc course *Aeroacoustics - 201800371*, at the faculty of Engineering Technology of the University of Twente. Enschede, 2020.

[21] Nikolaj Even, Thorben Koch, and Marcel Vliem. *Airfoil boundary layer characterisation by hot-wire anemometry*. As requisite of Leandro de Santana, professor, MSc course *Experimental Methods in Fluid Mechanics/Aerodynamics/Aeroacoustics - 202000245*, at the faculty of Engineering Technology of the University of Twente. Enschede, 2021.

[22] Glenn Research Centre. *Navier-Stokes equations*. National Aeronautics and Space Administration, Cleveland, OH, 2021.

[23] J. M. R. Graham. Similarity rules for thin aerofoils in non-stationary subsonic flows. *Journal of Fluid Mechanics*, 43(4):753–766, 1970. doi: 10.1017/S0022112070002719.

[24] Harry W. M. Hoeijmakers. *Lecture notes*, pages 13–24. University of Twente - Faculty of Engineering Technology, Enschede, 2014.

[25] F.P. Incropera and D.P. DeWitt. *Fundamentals of Heat Transfer*. Wiley, 1981. ISBN 9780471427117.

[26] Hrvoje Jasak. *Error Analysis and Estimation for the Finite Volume Method with Applications to Fluid Flows*. PhD thesis, Imperial College, London, June 1996.

[27] D. W. Kearney, W. M. Kays, R. J. Moffat, and R. J. Loyd. The effect of free-stream turbulence on heat transfer to a strongly accelerated turbulent boundary layer. Technical Report HMT-9, Thermosciences division / Department of Mechanical Engineering / Stanford University, Stanford, CA, February 1970. Supported by: The national science foundation (NSF GK-2201) & The National Aeronautics and Space Administration (NGR 05-020-134).

[28] Theodore von Kármán. Mechanische aenlichkeit und turbulenz. *Nachrichten von der Gesellschaft der Wissenschaften zu Göttingen, Mathematisch-Physikalische Klasse*, 1930:58–76, 1930. URL `http://eudml.org/doc/59299`.

[29] Francesco La Camera. Renewable power generation costs in 2022. Technical Report ISBN: 978-92-9260-544-5, International Renewable Energy Agency, Abu Dhabi, December 2023.

[30] S. Oerlemans, P. Sijtsma, and B. Méndez López. Location and quantification of noise sources on a wind turbine. *Journal of Sound and Vibration*, 299(4):869–883, 2007. ISSN 0022-460X. doi: https://doi.org/10.1016/j.jsv.2006.07.032.

[31] Dinah Achieng Ewuradjoa Ogara. Assessing the fluxes and impacts of drought-induced migration of pastoralist communities into urban areas : A case of marsabit town, northern kenya. Master's thesis, University of Twente, Enschede, February 2018.

[32] R Parchen. Progress report DRAW, a prediction scheme for trailing edge noise based on detailed boundary-layer characteristics. Technical Report HAG-RPT-980023, TNO institute of applied physics, Delft, February 1998.

[33] Allan Pierce. *Acoustics: An Introduction to Its Physical Principles and Applications*, volume 34. Springer, 06 1989. ISBN 0883186128. doi: 10.1063/1.2914388.

[34] Osborne Reynolds. Iv. on the dynamical theory of incompressible viscous fluids and the determination of the criterion. *Philosophical Transactions of the Royal Society of London. (A.)*, 186: 123–164, 1895. doi: 10.1098/rsta.1895.0004.

[35] Christopher Rumsey. *The Spalart-Allmaras Turbulence Model*. Langley Research Center - Turbulence Modeling Resource, Langley, US, 2024.

[36] Leandero de Santana, Martinus Sanders, Cornelis Venner, and Harry Hoeijmakers, editors. *The UTwente Aeroacoustic Wind Tunnel Upgrade*, AIAA/CEAS Aeroacoustics Conference, The UTwente Aeroacoustic Wind Tunnel Upgrade, 2018. American Institute of Aeronautics and Astronautics.

[37] Leandro de Santana. Fundamentals of acoustic beamforming. Technical Report STO-EN-AVT-287-04, North Atlantic Treaty Organization - Science & Technology Organization, May 2017.

[38] Joyce Schijven. Noise pollution and its effects on the SOFAR channel. Bachelor's thesis, University of Twente, Enschede, 2024.

[39] Philippe Spalart and Steven Allmaras. A one-equation turbulence model for aerodynamic flows. *AIAA*, 439, 01 1992. doi: 10.2514/6.1992-439.

[40] Stichting De Twickelrand. Steun onze actie tegen windmolens bij woonwijken van borne en hof van twente. Website - `https://geenwindmolensbijwoonwijken.nl/`, 2024. Accessed: 2024-07-02.

[41] Ricardo Vinuesa, Seyed Hosseini, Ardeshir Hanifi, Dan Henningson, and Philipp Schlatter. Pressure-gradient turbulent boundary layers developing around a wing section. *Flow Turbulence and Combustion*, 99:613–641, 12 2017. doi: 10.1007/s10494-017-9840-z.

[42] P. Welkers, E. van Kempen, R. Helder, E. Verheijen, and R. van Poll. Motie schonis en de whorichtlijnen voor omgevingsgeluid. Technical Report DOI 10.21945/RIVM-2019-0227, National Institute for Public Health and the Environment and the Dutch Ministry of Infrastructure and Water Management, Bilthoven, 2018.

[43] David Weyburne. A boundary layer model for unbounded flow along a wall. Technical Report AFRL-RY-WP-TR-2020-0004, Air Force research laboratory / Sensor directorate / Air Force Materiel Command / United Stated Air Force, Wrigth-Patterson Air Force base, OH, February 2020.

[44] Charles Wheatstone. Xiii. the bakerian lecture.—an account of several new instruments and processes for determining the constants of a voltaic circuit. *Philosophical Transactions of the Royal Society of London*, 133:303–327, 1843. doi: 10.1098/rstl.1843.0014.

[45] W.W. Willmarth and F.W. Roos. Resolution and structure of the wall pressure field beneath a turbulent boundary layer. *Journal of Fluid Mechanics*, 22(1):81 – 94, 1965. doi: 10.1017/S0022112065000599.

A Extraction from discretized solution

The solver used (SU2) does not directly output the data of interest. Mostly because the values are not primitive-, solution- or coordinate-field properties, but also because for most properties, not the entire domain is of interest.

A.1 Field output format

The solver outputs its solution field in a `.vtu` in a `config.cfg` specified location. This is not yet an ASCII readable file but can be opened in the visualization tool Paraview. In the current configurations, the command `VOLUME_OUTPUT= SOLUTION, RESIDUAL, SKIN_FRICTION-X, Y_PLUS, DENSITY, COORD-X, COORD-Y` results in the `.vtu` file to contain the properties in the following list to which the gradient of the pressure variable is added within Paraview.

- Density (ρ)
- Spallart-Allmaras turbulence transport variable ($\tilde{\nu}$)
- Pressure (P)
- Residual of the Spallart-Allmaras variable
- Residual of the pressure
- Residual of the velocity in 3 direction components
- Skin friction coefficient ($\vec{C_f}$) in 3 direction components
- Velocity ($\vec{u}$) in 3 direction components
- Non-dimensionalized normal distance (y^+) (only non-zero at non-slip boundary nodes)
- Pressure gradient ($\nabla(P)$) in 3 direction components

From these fields, an export to a comma-delimited ASCI readable file (`.csv`) can be made, but this would export the entire field in an unorganized manner and would increase the read and write time significantly, which is already a concern for these per line reading formats. As a solution, only the data points in the two main regions of interest are extracted.

A.1.1 Flat plate region

The first region of interest is the purely flat section of the boundary on the flat plate so for $0.2 \leq x \leq 0.9$ and covering a y-coordinate range of $0 \leq y \leq 0.03$. This domain is visualized in figure 25. Although the solver is default in SI units, the exported fields are mostly non-dimensionalized and therefore, the implied units for the coordinate system are in meters. Based on the first simulation results this y-coordinate domain covers the boundary layer profile well, as well as a part of the void left by the flat plate geometry. The latter, however, does not contain any data points and therefore does not contribute to the file size. In order to improve file structuring, a default name is given to all these export file: `bl_data.csv`.

The main advantage of exporting this region, is that it mainly consists of the structured grid type due to the boundary layer. Therefore, boundary layer profiles can be extracted efficiently due to the relatively constant y-coordinate value in the set of nodes. How this happens will be explained further in section A.2, but it is the main reason that the domain is limited to $0.2 \leq x \leq 0.9$.

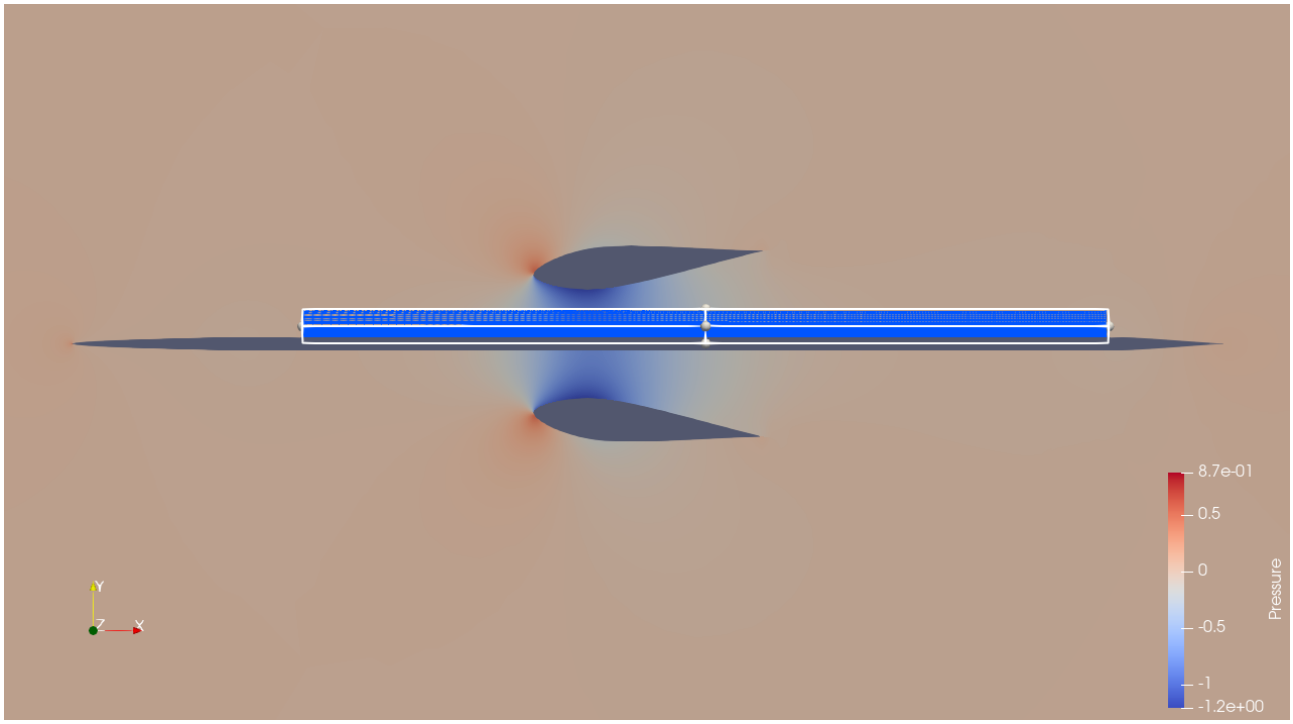

Figure 25: The white box section indicating the domain $0.2 \leq x \leq 0.9$ and $0 \leq y \leq 0.03$ and the exported nodes in blue.

A.1.2 Trailing edge cross-section

A second location of data extraction is the trailing edge, as the boundary layer properties there, are what eventually powers the noise mechanism of interest. While the cells at these positions are still built up in a mostly structured grid, this grid is no longer aligned with the y-axis. Therefore finding the correct nodes along a single cross-section among a wider set of nodes is far less straightforward. In order to resolve this issue an intersection extract is used where the nodes of cells are extracted that are intersected by a predefined line. This line is defined as $x = 1$ and $0 \leq y \leq 0.05$ to capture the boundary layer well. This region is visualized in figure 26 and the standardized export filename is: `tail_data.csv`.

A.2 Data import/post processing

The data handling occurs in the programming software `MatLab` where the selected file is read per line and then converted to a data matrix. The columns of this import matrix correspond to the field properties on the list of section A.1. As the script does not automatically read this the column identification has to be set by hand in advance. For the case of the flat plate region of figure 25, the boundary layer has to be sliced into sections with a constant value of the x-coordinate. However, due to the small deformation in the grid built-up, there is an immensely small deviation from perfectly rectangular cells as such sorting all data points per unique x-value would simply not work for the 15 decimal places export that is used. Therefore the column of x-coordinates is exported and rounded to the first three decimal places (approximately the discretization used in this section). From this array, all nodes are then sorted per unique value of this array. For each of these positions, an object is then created in the array `profiles(k)`, to which all nodes are added but is later also supplemented with calculated boundary layer property values.

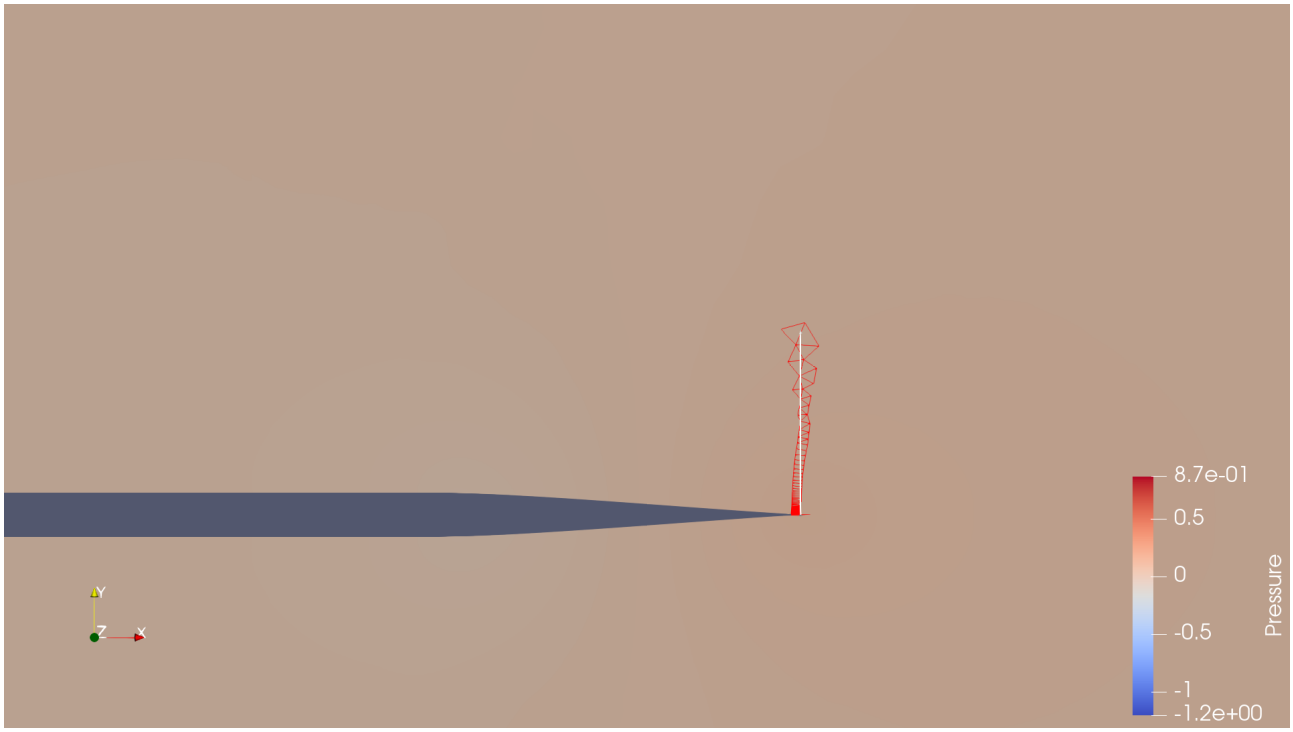

Figure 26: The white intersection line at $x = 1$ and $0 \leq y \leq 0.05$ and the exported nodes in red.

A.2.1 Velocity profile

By definition, it should be possible to fit a smoothing spline through the velocity data points as the fundamental continuity assumption coupled with the absence of shock behaviour should apply in this resolution. As such, the smoothing spline interpolation is applied for each valid profile (profiles for which the before-mentioned slicing was successful and thus contains sufficient nodes). Using this profile, the first boundary layer parameter can directly be resolved in an exact manner, namely the boundary layer thickness where the `fzero()` function can be applied to exactly find the condition $u = 0.99u_\infty$. It also results in a parametric function that can be analytically integrated with the calculation of the integral boundary layer parameters. The steps now mentioned are realized in code snippet 1.

Snippet 1: Creating a velocity profile function and finding the boundary layer thickness

```
1 if (length(profiles(k).xvel) ≥ 3)
2     profiles(k).xvel = profiles(k).xvel([1 3:end 2]);
3     profiles(k).ypos = profiles(k).ypos([1 3:end 2])-min(profiles(k).ypos);
4     profiles(k).xvel_fit = fit(profiles(k).ypos,profiles(k).xvel,'smoothingspline');
5     profiles(k).u_inf = profiles(k).xvel_fit(exp_far);
6     profiles(k).Δ = fzero(@(x) ...
          profiles(k).xvel_fit(x)-0.99*profiles(k).u_inf,exp_far./2);
7 else
8     profiles(k).skip=true;
9 end
```

A.2.2 y-value independent properties

For each slice of the boundary layer, some properties, are assumed to be constant or are a boundary property. In the next section of code, these properties are extracted and added to the `profiles(k)` object. In snippet 2, the first property to be extracted is c_f which should only have a non-zero component in the boundary node. From the `csv` raw import variable, the nodes pertaining to this cross-section are first selected and then in the second line the non-zero item from the previous array is saved. As it is assumed that the pressure gradient along the x-axis always far exceeds that in along the y-axis and the thickness of the boundary layer is relatively small. The pressure is assumed to be constant through the boundary layer, therefore, the non-dimensionalized pressure is averaged over the nodes and multiplied by the reference pressure defined at the global domain inflow boundary. This value can be extracted from the console output of the used solver (`SU2`). This dynamic reference pressure has often been $5444.34\frac{N}{m^2}$ and is consequently also what can be used in dimensionalizing the shear stress and for the calculation of the shear velocity u_τ. For the latter also the local density is needed but this can also be taken from the inflow condition as $\rho_\infty = 1.2886\frac{kg}{m^3}$ since the solver is set to incompressible (mode).

Snippet 2: Creating a velocity profile function and finding the boundary layer thickness

```
1 profiles(k).cf = csv(find(csv(:,x_i) == profiles(k).xpos),cf_i);
2 profiles(k).cf = max(unique(profiles(k).cf));
3 %assuming constant pressure through bl
4 profiles(k).p = mean(csv(find(csv(:,x_i) == profiles(k).xpos),p_i)).*dyn_p_ref;
5 profiles(k).t_w = profiles(k).cf*dyn_p_ref;
6 profiles(k).u_tau = sqrt(profiles(k).cf*dyn_p_ref./rho_ref);
```

A.2.3 Integral boundary-layer parameters

The integral boundary layer parameters mentioned in section 3.1 are calculated in code snippet 3. In the first line, a function `u_norm(y)` is created which is the function $U(y)$ from section 3.1. Then in lines two and three, deficit functions for velocity and specific momentum are defined based on the integrands of equations 14 and 15. In lines four and five, these integrals are then also evaluated where it should be remarked that the y-position can not be used in the limits as the flat plate itself has a non-zero y-value. A translation could be applied but it was found to be more convenient to set the lower integration bound to zero and the upper to the earlier established boundary layer thickness.

Snippet 3: Calculation of the integral parameters

```
1 u_norm = @(y) (profiles(k).xvel_fit(y))./profiles(k).xvel_fit(profiles(k).Δ);
2 d1fun = @(y) 1-u_norm(y);
3 d2fun = @(y) d1fun(y).*u_norm(y);
4 profiles(k).d1 = integral(d1fun,0,profiles(k).Δ,'arrayvalued', true);
5 profiles(k).d2 = integral(d2fun,0,profiles(k).Δ,'arrayvalued', true);
6 profiles(k).H = profiles(k).d1/profiles(k).d2;
7 profiles(k).G = (1-1./profiles(k).H).*profiles(k).u_inf./profiles(k).u_tau;
```

This upper limit theoretically should have little impact, as the integrand should diminish near the upper limit, due to the fact that there is no longer a build-up of deficit. This, however, only applies to the case where the far-field velocity behaves reasonably constant outside the boundary layer. While the integral parameters are a direct result of the deceleration due to the no-slip condition, this is not the only feature that can create a velocity gradient perpendicular to the surface. Capturing these other contributions might, however, give a false impression and therefore code snippet 4 is introduced to study the effect of a possibly incorrectly defined boundary layer thickness. It is the expectation that all parameters should be relatively stable in the current limit indicating some form of uniform far-field velocity (although possibly only local).

Snippet 4: Calculation of the integral parameters

```
for k = 1:length(int_lim_arr)
    d1_il(k) = integral(d1fun,0,int_lim_arr(k),'arrayvalued', true);
    d2_il(k) = integral(d2fun,0,int_lim_arr(k),'arrayvalued', true);
end
plot(int_lim_arr,d1_il./d2_il) %plotting
plot(profiles(prof_sel).Δ,profiles(prof_sel).H,'*') %plotting the selected limit
```

In snippet 4, the functions `d1fun` and `d2fun` are previously selected from snippet 3. Then the array `int_lim_arr` is defined for a range that is likely of interest without taking zero as a solution, as this would result in a divide by zero error when calculating the shape factor. The current range is set by `int_lim_arr = linspace(0.0005,0.01,80)` resulting in figure 27 from configuration 13 in table 3. Meanwhile, the command `savefig([folder 'int_limit.fig'])` results in the saving of this check as default when the check is enabled (even when applied in an array of simulations).

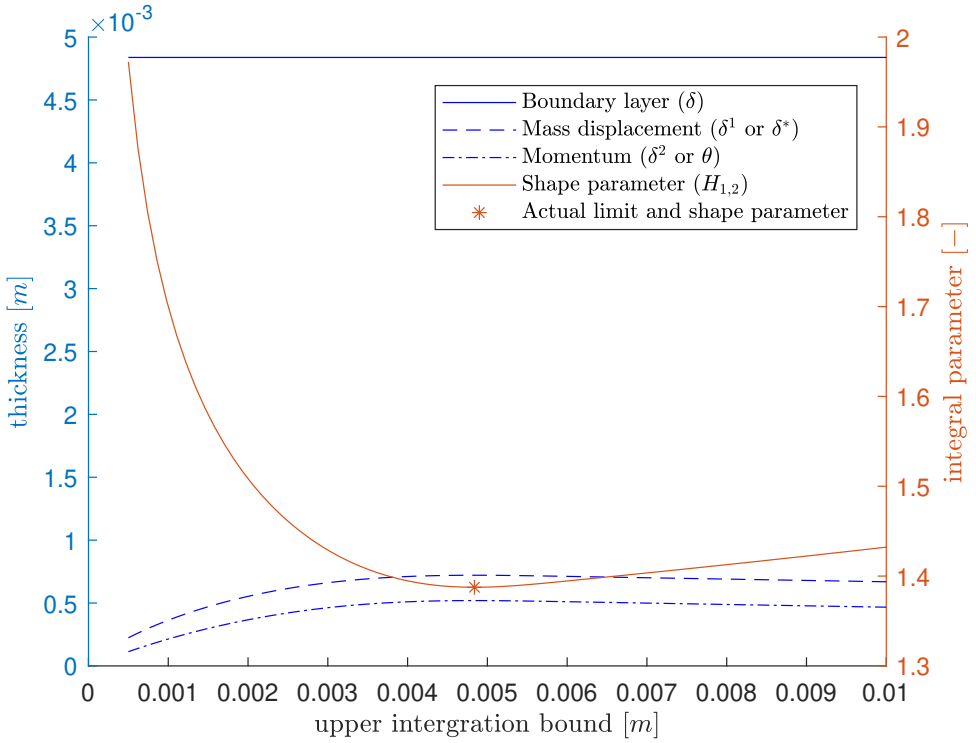

Figure 27: Effect of the upper integration limit in the calculation of the boundary layer integral parameters, applied to configuration number 13 in table 3.

From figure 27, it appears all values are close to their minima of maxima, increasing the likeliness that some form u_∞ is indeed approached at the upper integration limit, while it also directly confirms the turbulent character of the boundary layer based on the found shape factor ($H_{1,2}$).

A.2.4 Non-dimensionalized pressure gradient

The final piece of data to be extracted is the non-dimensionalized pressure gradient as mentioned in section 3.2.1 which can be calculated using snippet 5. The pressure gradient in x-direction added in Paraview is normalized here with a combination of the shear stress of snippet 2 and mass displacement thickness of snippet 3.

Snippet 5: Calculation of the non-dimensionalized pressure gradient

```
1 profiles(k).brc = profiles(k).d1./profiles(k).t_w*mean(profiles(k).grad_p);
```

A.3 Combining multiple simulations

It has been desirable to not convert the designed scripts to functions as the input from different sections of code has been proven useful in the workspace. Therefore in script `group_analysis.m` a consistent set of variables is used that are not cleared in the scripts `analysis.m` and `wake_analysis.m` so that they remain in the workspace. As a result the `clear` command is substituted for the command `clearvars -except folder name cash_name wake_cash_name`. At the end of the scripts `analysis.m` and `wake_analysis.m`, the results are written to the `.mat` variables defined at the beginning of the script `group_analysis.m`. With this system for every simulation, a name and run folder can be specified out of which the files `bl_data.csv` and `tail_data.csv` are then retrieved. In the last part of the script `group_analysis.m` the `.mat` files can then be reloaded and a the results of multiple simulations can then be combines in singular visual representations as shown in section 5.3.

B The beamformer technique applied to acoustics

As mentioned before, the acoustic beamformer technique is similar to how radar systems work, but this section explains how that would apply to sound. Starting with the equipment needed, typical set-ups for acoustic beamformers consist of an array of microphones distributed in space. Isolating the equipment needed for a single microphone, Santana identifies a set of core components to be included in the schematic overview of figure 28[37].

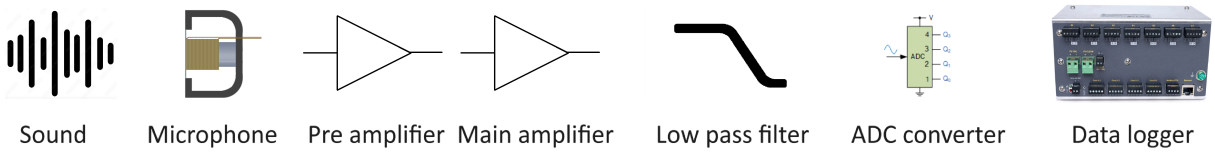

Figure 28: Schematic representation of the microphone data acquisition system.

In this overview, the sound is captured with the microphone transducer, however, this signal does not carry a lot of energy so to decrease the influence of electromagnetic noise it is directly pre-amplified so that it can be transported reliably. After transport, it is amplified in a more efficient central analog amplifier after which it passes through a low-pass filter before being converted to a digital signal. This is needed, as real-world signals almost inevitably contain some unwanted high-frequency behaviour. If the frequency of this behaviour exceeds the limits of the analog-to-digital converter then aliasing might occur. A low-pass filter solves this issue as long as the acquisition system of figure 28 is at least able to capture the relevant frequency behaviour expected.

Once the digital pressure signals of the microphones are stored in an analysis system, the actual beamformer can be applied. But in this application, some assumptions are made. In aeroacoustics, all noise sources will typically be represented by a combination of mono-, di- and quadru-pole sources [13], but in the cases of these beamformers, it is assumed that the distance between the microphone array and the noise source is so large compared to the distance between the microphones in the array that the directivity of the sources can be neglected and all sources are regarded as monopoles (q, without directivity). This is called the acoustic far-field. Next, the acoustic wave propagation can exactly be described by the Navier-Stokes equations as used before in section 3.1, but since it is reasonable to assume linear and isentropic behaviour [33], they can be significantly reduced to the Helmholtz wave equation given in equation 49. In this equation, it is visible how the signal decays proportional to the increasing distance from the microphone array. Besides that, it also indicates the time retardation due to signal travelling. Since this occurs under a constant velocity (c_0), this time retardation can be expressed as a function of distance in equation 51 also referred to as the retarded time.

$$\left(\frac{1}{c_0}\frac{\partial^2}{\partial t^2} - \nabla^2\right) p = q(t)\delta(\vec{x} - \vec{x}_0) \tag{49}$$

$$p(\vec{x}, \vec{x}_0, t) = \frac{1}{4\pi}\frac{q(\vec{x}_0, t - |\vec{x} - \vec{x}_0|/c_0)}{|\vec{x} - \vec{x}_0|} \tag{50}$$

$$t_0 = \frac{|\vec{x} - \vec{x}_0|}{c_0} \tag{51}$$

The most basic form of the beamformer technique is the conventional beamformer (delay and sum beamformer). If a point in space ($\vec{x}$) is selected, then the distance to every microphone is likely different. This difference is captured in the retarded time as given in equation 51. If this location is then close to a sound source, all the waves to which the time retardation is correctly applied combined will result in constructive interference while destructive interference will occur when regarding other positions. This combining action occurs in a summation and results in equation 52 for the output map of this method. In this equation, M indicates the number of microphones in the array and the final term is normalizing the effect of the signal decay over distance.

$$L(t, \vec{x}_0) = \frac{4\pi}{M} \sum_{m=1}^{M} p_m(\vec{x}_0, t + t_0)|\vec{x} - \vec{x}_0| \tag{52}$$

When subjected to a point source, the output mapping is referred to as the point spread function as it gives an impression of the parasitic effects in the output map isolating a single input contribution. Such a function would look similar to figure 29, which is created from a single monopole analytical benchmark file [5], using a conventional beamformer at $f = 500Hz$[20]. As the name suggests only a single mono-pole is present in the input data, though, besides the global maximum (around zero decibels) more local maxima can be identified. These local maxima are designated as side lobes and the ratio between the main lobe (at the global maximum) and the side lobes (at other local maxima) is very fittingly referred to as the main-to-side-lobe ratio. This ratio indicates the ability of the system to identify different source amplitudes. Looking at the main lobe itself, its width is also of interest as the noise source is a point source. It is the convention to look at the width of the lobe $3dB$ below its maximum, which is referred to as the beam width. This parameter indicates the spatial resolution achievable by the system. For example, if the beam width is larger than the distance between two point sources, it is likely that they will appear as a single source.

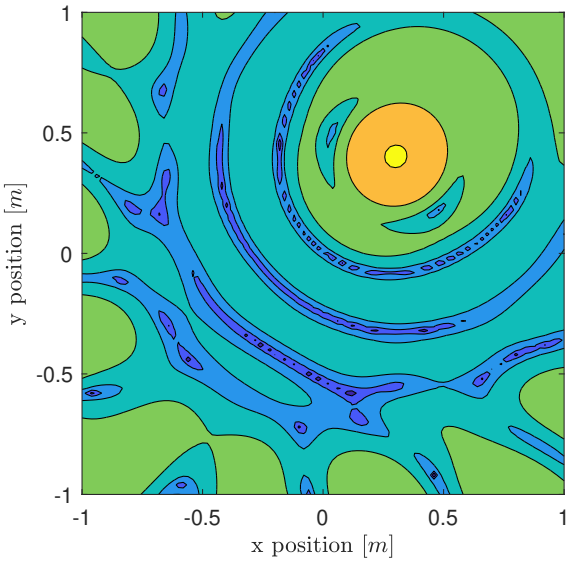

Figure 29: Countour plot of a typical point-spread function between $-30dB$ (represented by the dark blue) and $0dB$ represented by the yellow.

Unfortunately, the delay sum beamformer has a quite poor main-to-side-lobe ratio and a quite poor spatial resolution. In addition, applying efficient post-processing techniques to resolve these issues is hard and thus an alternative was created. By transferring the problem to the frequency domain a so-called frequency domain beamformer can be constructed (given in equation 53).

$$P(\vec{x}, \vec{x}_0, \omega) = \mathcal{F}(p(\vec{x}_0, t + t_0)) = \int_{-\infty}^{\infty} p(\vec{x}_0, t + t_0) e^{i\omega\tau} d\tau \tag{53}$$

[5] File accessible via: `https://universiteittwente-my.sharepoint.com/:u:/g/personal/m_j_h_vliem_student_utwente_nl/EZKel4XVCcBJpPDXzsupz4YBPCUEkcBF2Jpb8idhqPw60A?e=tP8Sdg`

C Hot-wire anemometry

Hot-wire anemometry was used to measure time-averaged velocity and its fluctuation. This technique combines a dependence of electrical resistance on temperature, with the cooling effect of forced convection. In very short terms, the velocity at each moment is determined by the amount of power that can be convected away from a probe [21].

In measuring the amount of electrical power, Pouillet's law gives an expression (equation 54) of the electrical resistance over the probe wire, where ρ is the resistivity, l is the length of the wire and A the wire cross-section. Next, it is assumed that $l >> A$ and that thermal expansion therefore is isolated to l, with its contribution to A being disregarded. As such, the equation for the linear expansion of metals in equations 55 can be combined with equation 54 to create an expression of electrical expansion based on the temperature (equation 56), where R_{w_0} is the calibration resistance at temperature T_0 and α is the thermal expansion coefficient.

$$R = \rho \frac{l}{A} \tag{54}$$

$$l = l_0(1 + \alpha_0(T_w - T_0)) \tag{55}$$

$$R_w = R_{w_0}(1 + \alpha_0(T_w - T_0)) \tag{56}$$

By applying a Wheatstone bridge [44], the varying resistance of the wire can be translated to the varying voltage which can be regulated relatively fast. Unfortunately, there is a parasitic heat transfer mechanism present in the wire: The conduction to the prong holding the wire. As such, a more uniform temperature along the wire results in a higher ratio of heat being convected by the air over heat being conducted through the prong. Naturally, this is the case for a high wire length (spreading the temperature gradient), low thermal conductivity (requiring a high gradient) and high conductivity (and thus equation 57). As a high Biot number is desired and an easy measure that can be taken is a high aspect ratio of the wire (increasing L), this high aspect ratio can also be used as an approximation in the modelling of the Nusselt number in equation 58 and eventually in an expression of the electric load as a function of the flow velocity called King's law [5] as given in equation 59. In these equations, the fitting parameters A, B and n are typically calibrated using a pitot tube and varying the free stream velocity, while in this application a fourth order polynomial fit is applied as suggested by Bruun. This should suffice as the parameter n is not expected to exceed four.

$$Bi = \frac{h}{k} L \tag{57}$$

$$Nu(Re) = A^+ + B^+ Re^n \tag{58}$$

$$I_w^2 R_W^2 = E^2 = A + Bu^n \tag{59}$$

Next to the fitting parameters of King's law, the system responsiveness also needs to be verified. In this verification, a step input of the servo amplifier is applied to the wire. The amount of time needed to then return to the equilibrium temperature is a measure of the responsiveness and is expressed in the settling time τ_w which is defined as the time it takes to restore 97% of the step excitation. Meanwhile, keeping the undershoot within 15% of this excitation is common practice. This all results in the cut-off frequency (f_c) as defined in equation 60. Any time effects above this frequency can not accurately be measured as the system is not fast enough to capture them properly. Since any higher frequency behaviour still present in the signal is therefore by definition noise it will be filtered out with a low-pass filter.

$$f_c = \frac{1}{1.3\tau_w} \tag{60}$$

D Additional result visualizations

D.1 Empirical velocity profiles

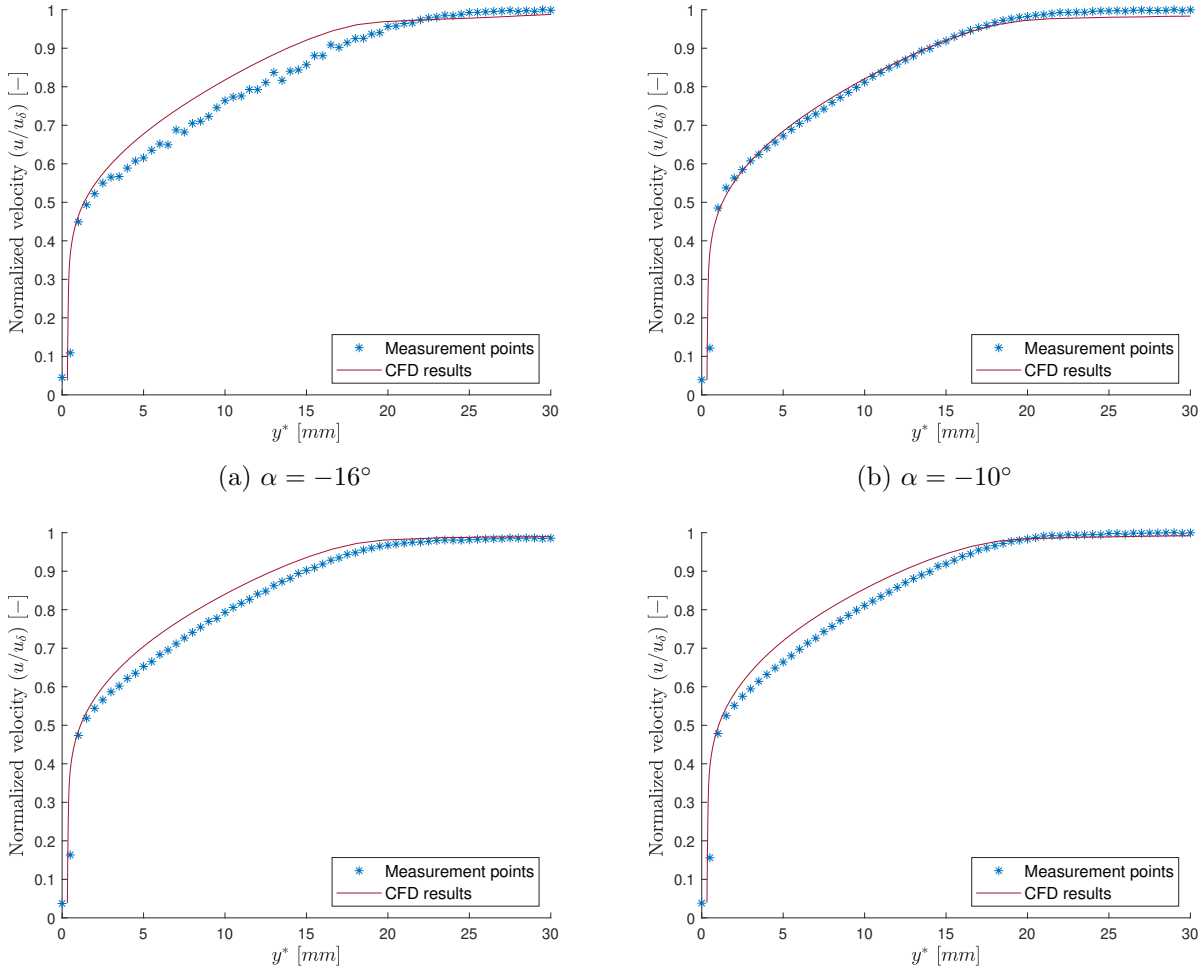

(a) $\alpha = -16°$

(b) $\alpha = -10°$

(c) $\alpha = -6°$

(d) $\alpha = -4°$

Figure 30: Boundary layer velocity profiles at the flat plate trailing edge against the normal distance (y^*) for negative angles of attack of the pressure gradient generating airfoils

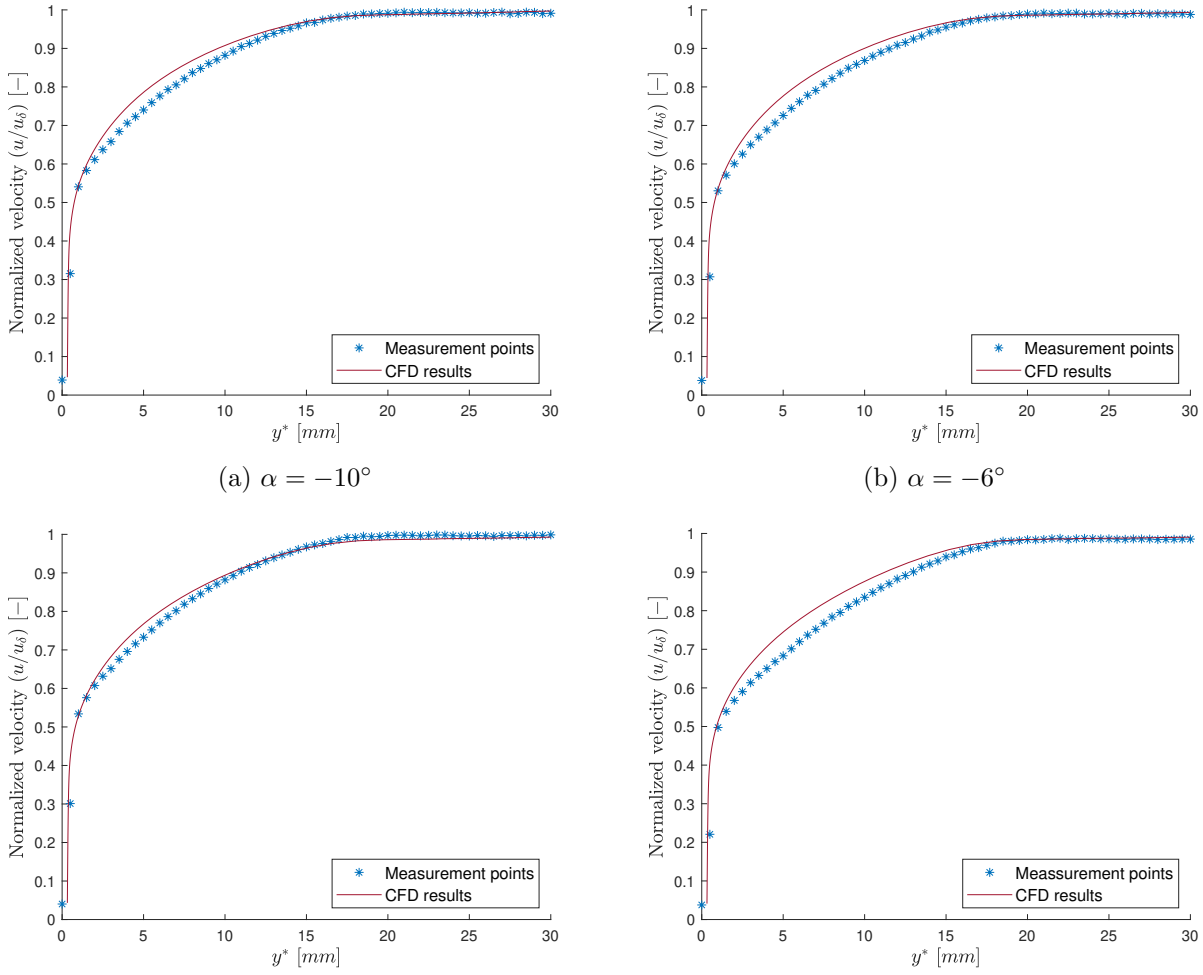

(a) $\alpha = -10°$

(b) $\alpha = -6°$

(c) $\alpha = -4°$

(d) $\alpha = 0°$

Figure 31: Boundary layer velocity profiles at the flat plate trailing edge against the normal distance (y^*) for positive angles of attack of the pressure gradient generating airfoils

D.2 Boundary layer integral parameters

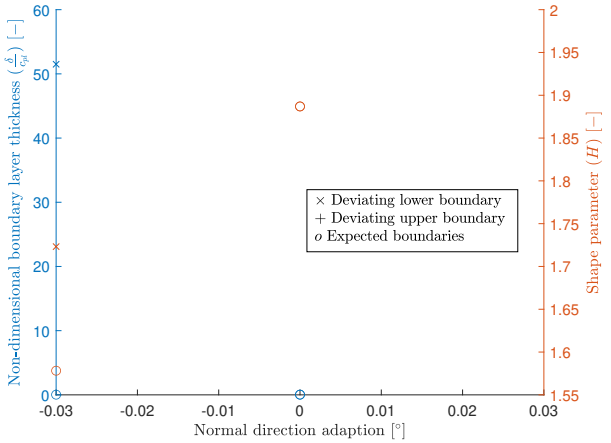

(a) Full set of properties against normal distance for $AoA = -6°$.

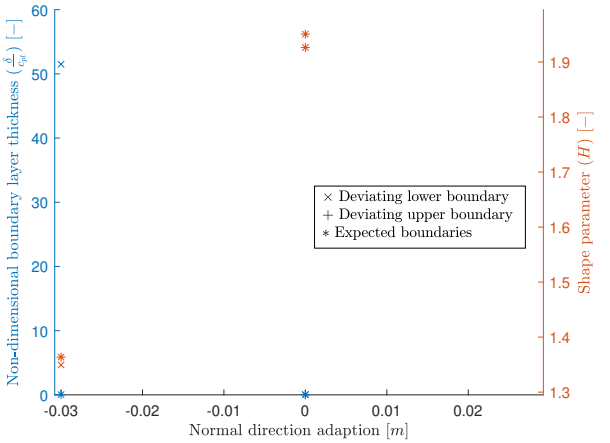

(b) Full set of properties against normal distance for $AoA = -10°$.

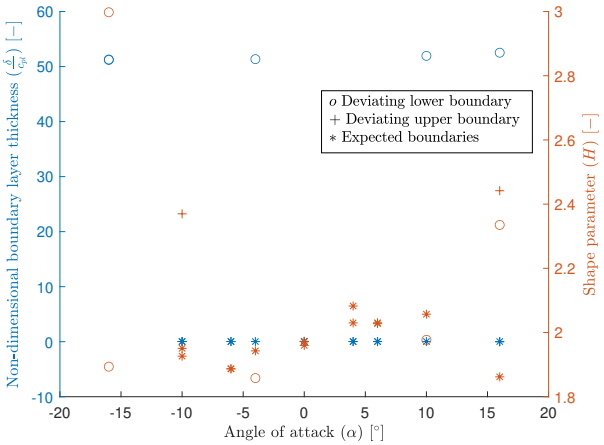

(c) Full set of properties against the angle of attack.

Figure 32: Unfiltered boundary layer integral properties (δ and H) at the trailing edge at the default height of $y = 0.1m$.

D.3 Flat plate pressure coefficient distribution

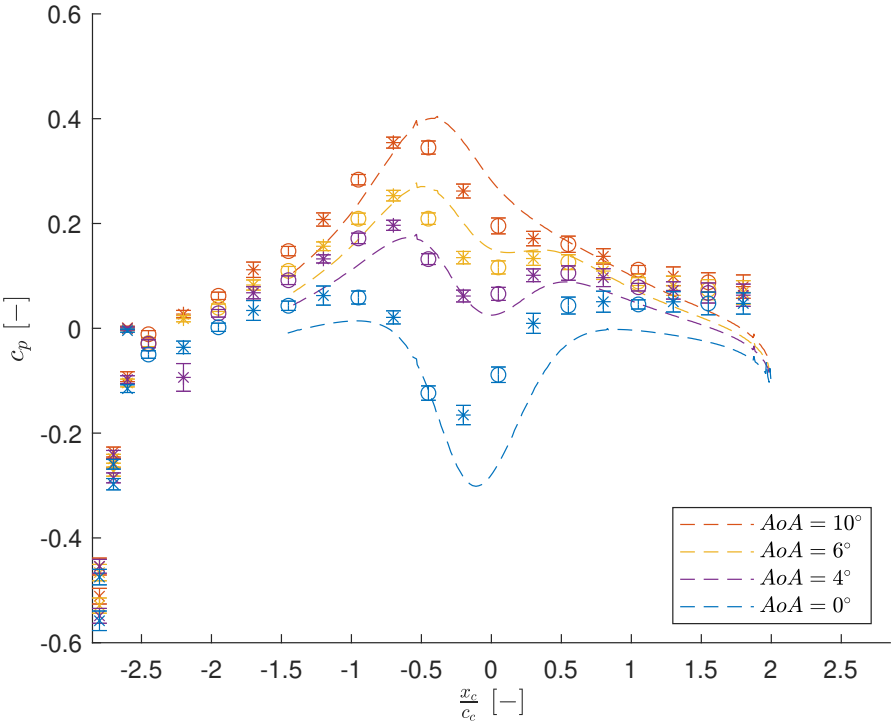

(a) Positive angles of attack.

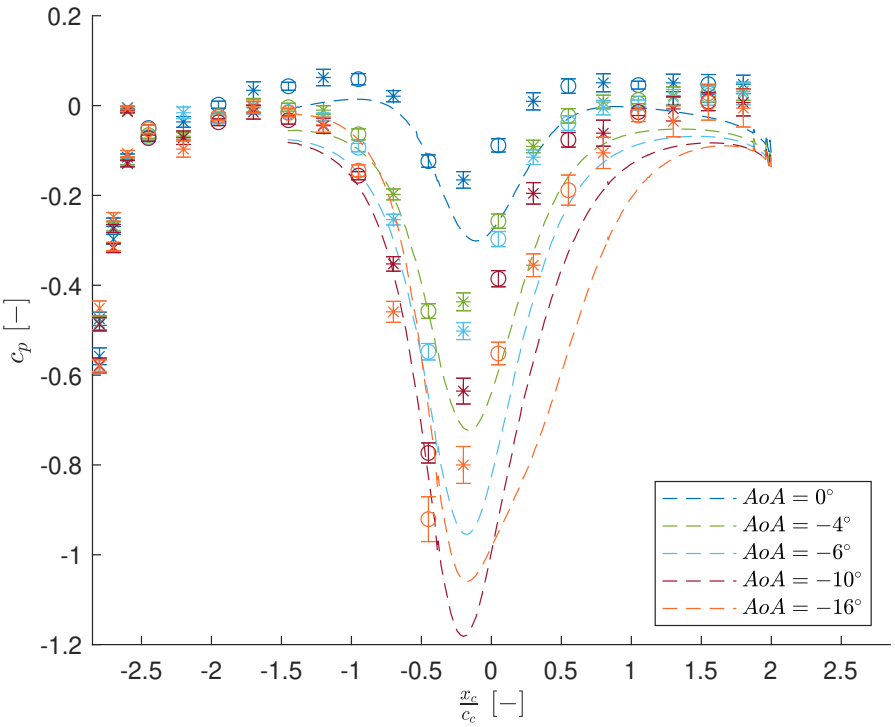

(b) Negative angles of attack.

Figure 33: Pressure coefficient along the flat plate with multiple angles of attack of the pressure gradient generating airfoils. Plotted against the x position on the flat plate with zero indicating the axis of rotation of the pressure gradient generating airfoils ($x_c = 0$). This is normalized by the chord length of these airfoils (c_c).

D.4 Far-field beamformer maps

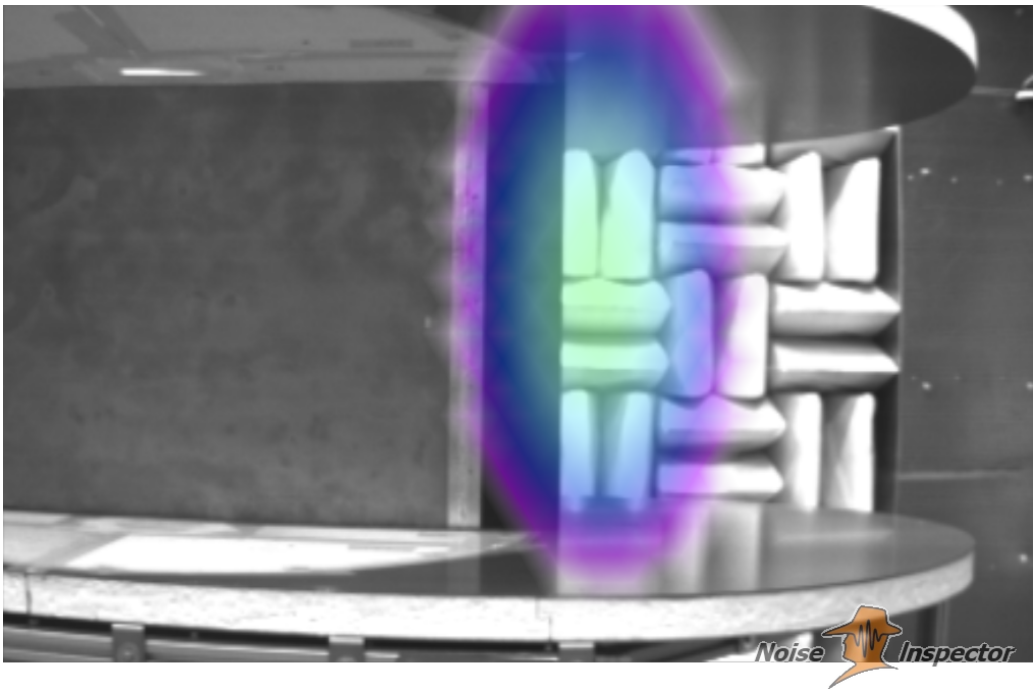

(a) Flat plate only

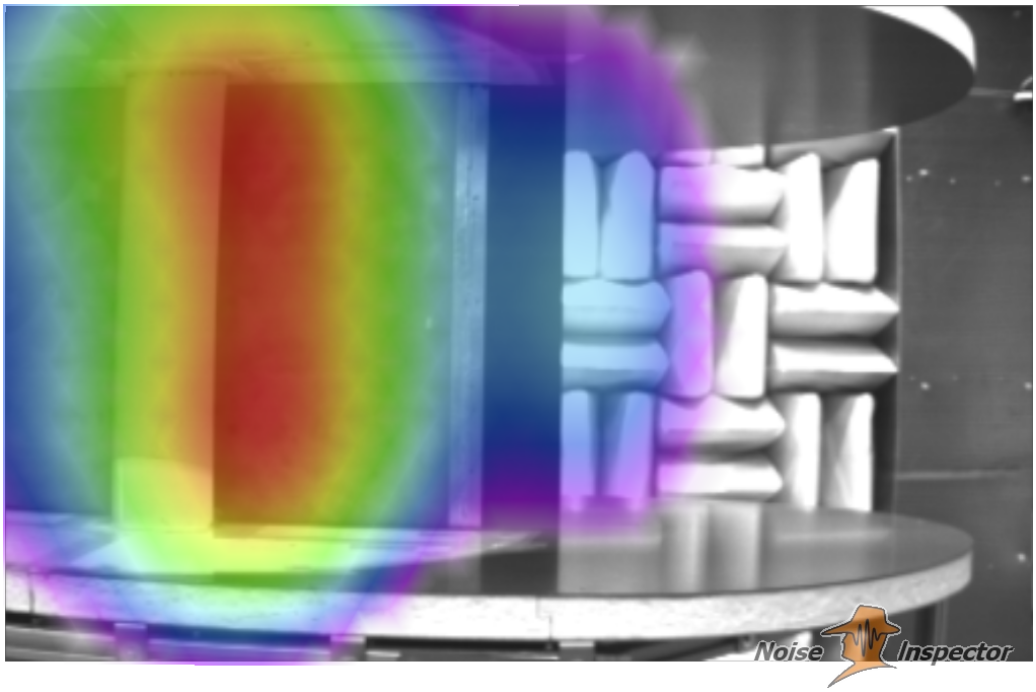

(b) External airfoils at zero angle of attack

Figure 34: Basis beamformer output maps with and without pressure gradient generating airfoils at zero angle of attack. The scales of the output maps are from $52.5dB$ (purple) till $58.5dB$ (red) using $p_{ref} = 2*10^{-5}Pa$. The frequency bin is $1500Hz < f < 2500Hz$ and the distance from the microphone array to investigative plane is $L = 2.01m$.

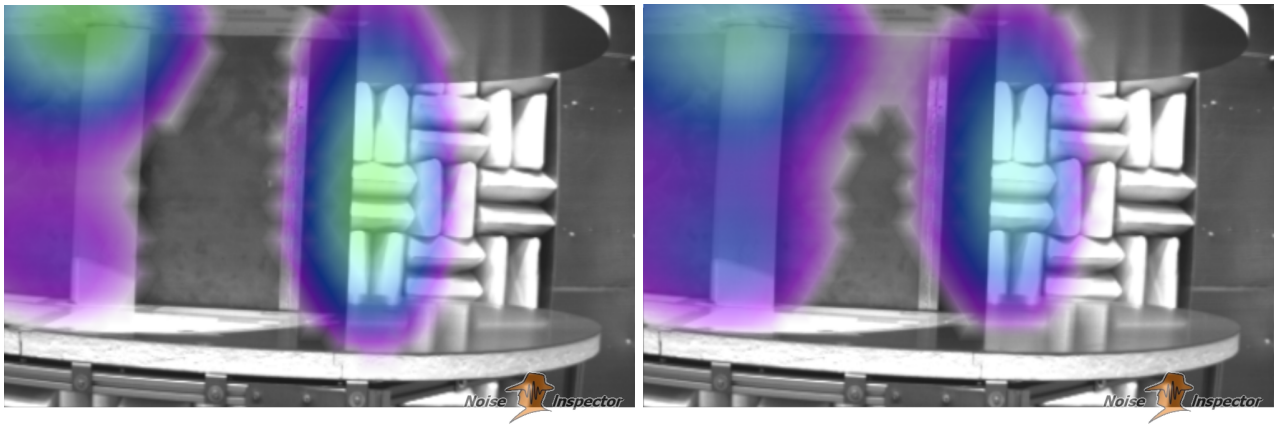

(a) $\alpha = 10°$ (b) $\alpha = 6°$

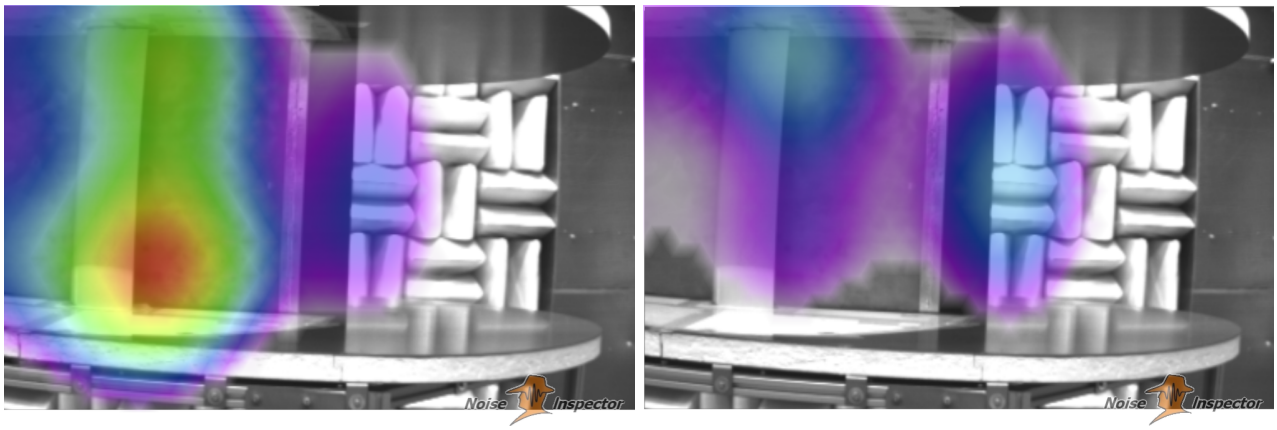

(c) $\alpha = -4°$ (d) $\alpha = -6°$

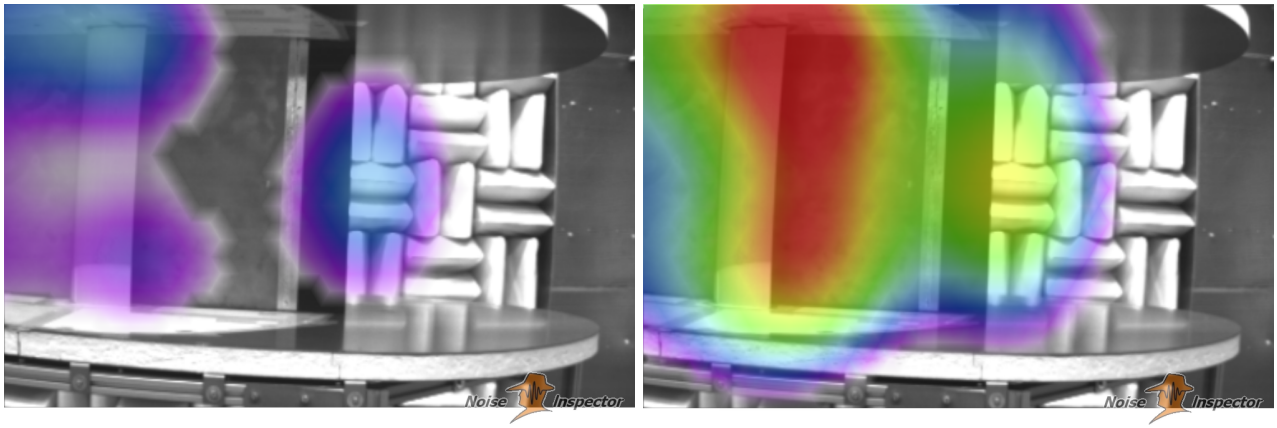

(e) $\alpha = -10°$ (f) $\alpha = -16°$

Figure 35: Beamformer output maps with the pressure gradient generating airfoils at various angles of attack. The scales of the output maps are from $52.5dB$ (purple) till $58.5dB$ (red) using $p_{ref} = 2 * 10^{-5}Pa$. The frequency bin is $1500Hz < f < 2500Hz$ and the distance from the microphone array to the investigative plane is $L = 2.01m$.

D.5 Numerical velocity profiles

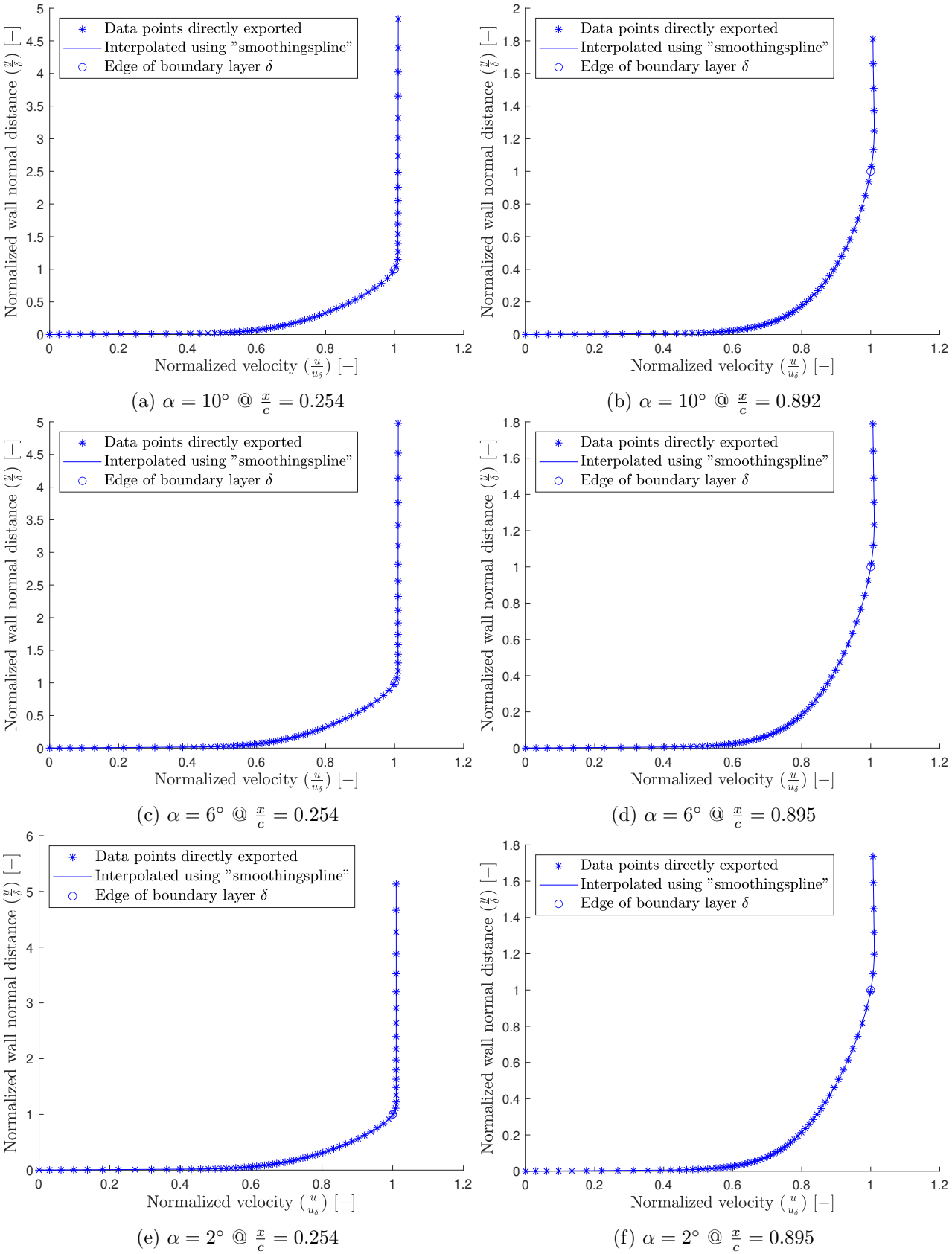

(a) $\alpha = 10°$ @ $\frac{x}{c} = 0.254$

(b) $\alpha = 10°$ @ $\frac{x}{c} = 0.892$

(c) $\alpha = 6°$ @ $\frac{x}{c} = 0.254$

(d) $\alpha = 6°$ @ $\frac{x}{c} = 0.895$

(e) $\alpha = 2°$ @ $\frac{x}{c} = 0.254$

(f) $\alpha = 2°$ @ $\frac{x}{c} = 0.895$

Figure 36: Boundary layer velocity profiles from CFD-SA results for the turbulent layer along the flat plate with the pressure generating airfoils being at positive angles of attack and default location as described in section 5.1.2

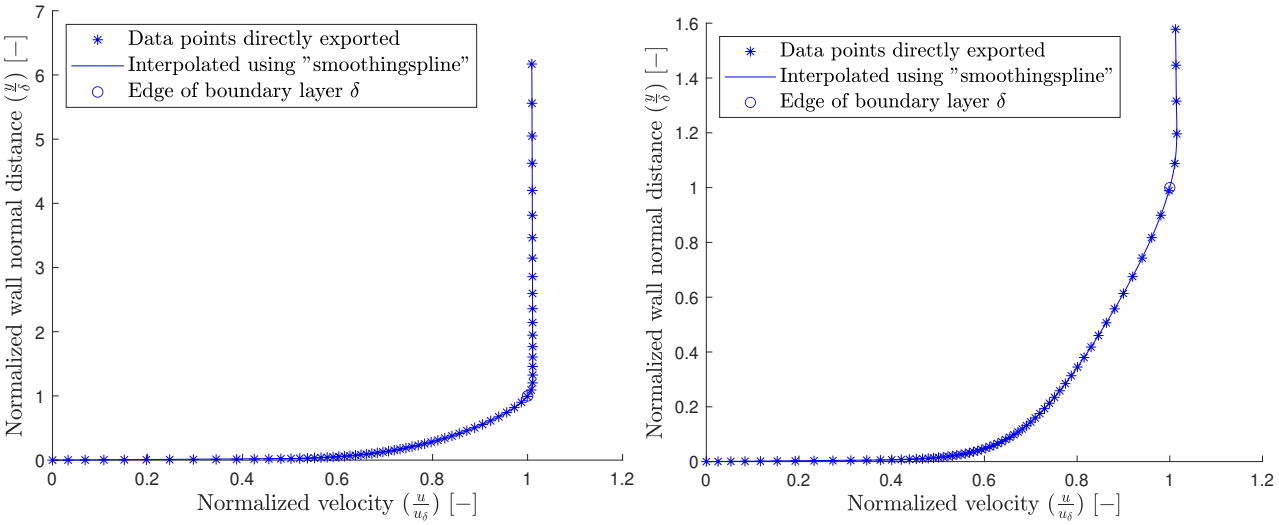

(a) $\alpha = -10°$ @ $\frac{x}{c} = 0.247$

(b) $\alpha = -10°$ @ $\frac{x}{c} = 0.892$

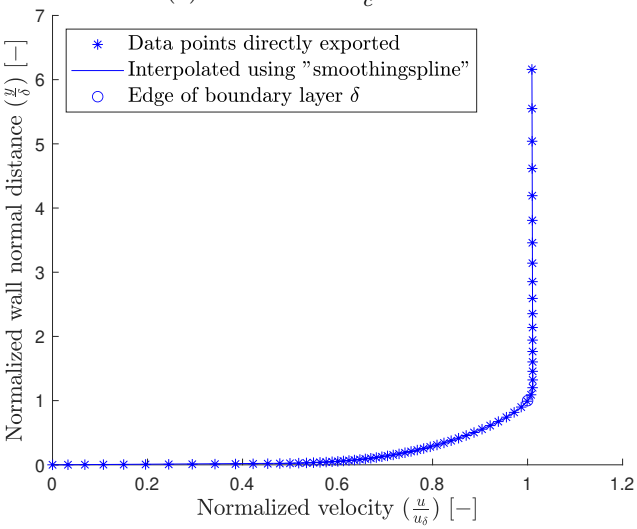

(c) $\alpha = -6°$ @ $\frac{x}{c} = 0.247$

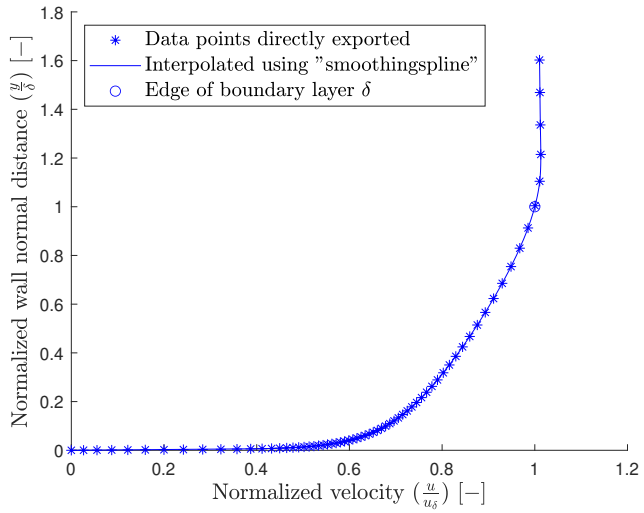

(d) $\alpha = -6°$ @ $\frac{x}{c} = 0.892$

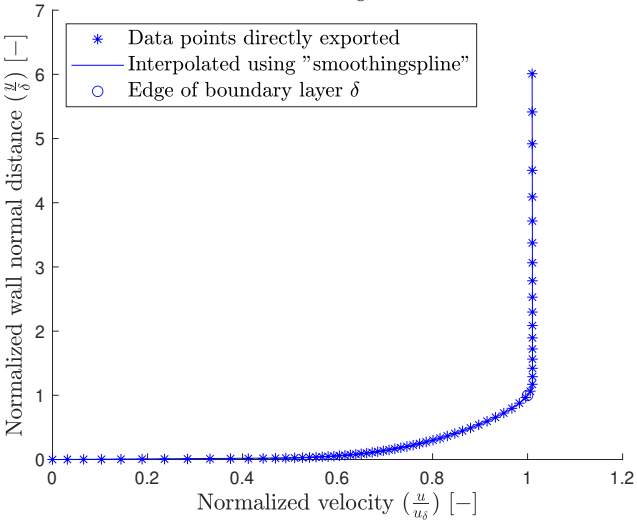

(e) $\alpha = -2°$ @ $\frac{x}{c} = 0.247$

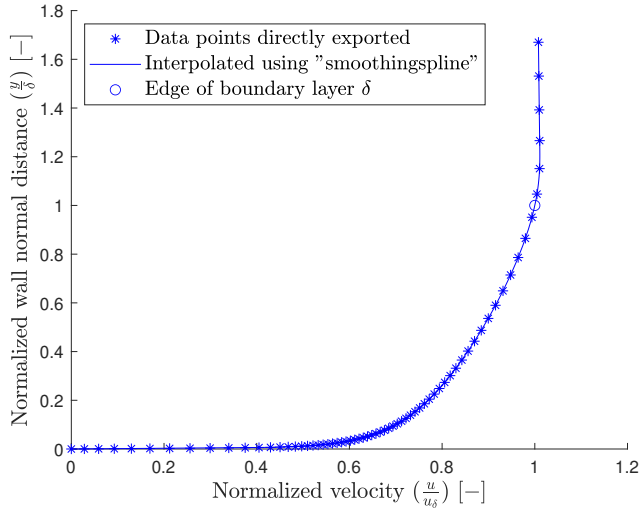

(f) $\alpha = -2°$ @ $\frac{x}{c} = 0.892$

Figure 37: Boundary layer velocity profiles from CFD-SA results for the turbulent layer along the flat plate with the pressure generating airfoils being at negative angles of attack and default location as described in section 5.1.2